Fracture Permeability Estimation Under Complex Physics: A Data-Driven Model Using Machine Learning

Xupeng He, Marwah M. AlSinan, Dr. Hyung T. Kwak and Dr. Hussein Hoteit

Abstract /

The permeability of fractures, including natural and hydraulic, are essential parameters for the modeling of fluid flow in conventional and unconventional fractured reservoirs. Traditional analytical (Cubic Law-based) models used to estimate fracture permeability show unstable performance when dealing with different complexities of fracture cases. This work presents a data-driven, physics included model based on machine learning as an alternative to traditional methods.

The workflow for the development of the data-driven model includes four steps.

1. Identify uncertain parameters and perform Latin Hypercube Sampling (LHS). We first identify the uncertain parameters that affect the fracture permeability. We then generate training samples using LHS.
2. Perform training simulations and collect inputs and outputs. In this step, high-resolution simulations with parallel computing for the Navier-Stokes (NS) equations are run for each of the training samples. We then collect the inputs and outputs from the simulations.
3. Construct an optimized data-driven surrogate model. A data-driven model based on machine learning is then built to model the nonlinear mapping between the inputs and outputs collected from Step 2. Herein, artificial neural network (ANN) coupling with the Bayesian optimization algorithm is implemented to obtain the optimized surrogate model.
4. Validate the proposed data-driven model. In this step, we conduct blind validation on the proposed model with high fidelity simulations.

We further test the developed surrogate model with newly generated fracture cases with a broad range of roughness and tortuosity under different Reynolds numbers. We then compare its performance to the reference NS equation solutions. Results show that the developed data-driven model delivers a good accuracy, exceeding 90% for all training, validation, and test samples. This work introduces an integrated workflow for developing a data-driven, physics included model using machine learning to estimate fracture permeability under complex physics, e.g., inertial effect.

To our knowledge, this technique is introduced for the first time for the upscaling of rock fractures. The proposed model offers an efficient and accurate alternative to the traditional upscaling methods that can be readily implemented in reservoir characterization and modeling workflows.

Introduction

Equivalent continuum and discrete fracture models are generally used for modeling fluid flow in fractured reservoirs at field-scale. The proper application of these models requires an accurate assessment of the permeability of rock fractures as input. The permeability of a rock fracture is a complex function of various static parameters, such as mean aperture, roughness, and contact areas, all of which are subjected to the dynamic stress acting on the fracture walls[1]. Herein, we investigate the relationship between fracture permeability and static parameters.

The full physics Navier-Stokes (NS) equations provide the most accurate approach for estimating the permeability of rock fractures[2]. Its expensive computational cost makes it infeasible for real applications[3]. In addition, experimental measurements are even more time-consuming.

Typically, discrete rock fractures have been idealized as two smooth, parallel plates with constant distance[4]. Based on this assumption, the NS equations lead to the well-known Cubic Law (CL). The CL has been widely used in various disciplines, including hydrology and petroleum, due to its simplicity and efficiency; however, the CL generally overshoots the hydraulic properties of rock fractures[5], as rock fractures are formed by two rough surfaces with variable apertures. Subsequently, various CL-based models have been developed in the literature for improving the accuracy of classical CL. These models could be categorized into two kinds: (1) by modifying the definition of the aperture used in the CL, such as arithmetic mean[5], geometric mean[6], and harmonic mean[7], and (2) by incorporating correction factors for fracture roughness[6, 8-12], flow tortuosity[5], and combined effect of

roughness and tortuosity[3, 13].

These models, however, show unstable performance when dealing with different complexities of fracture cases. In addition, all these models assume the laminar flow regimen and don't include complex physics within rock fractures, i.e., ignoring the inertial effect. To our knowledge, only one empirical model developed by Xiong et al. (2011)[14] was found in the literature to account for the inertial effect. This empirical model is obtained by fitting with a limited amount of data, which makes its broad applicability questionable. All these traditional models discussed here exhibit different levels of limitations, which inspires us to develop a big data-driven, physics included model for estimating the permeability of rock fractures.

Recent advances in machine learning have revolutionized many industries. They show that provided with a high-quality data set, a well-designed network structure, and proper hyperparameters, this technology is competitive to traditional models in terms of accuracy and efficiency. As a result, it inspires various geoscience and petroleum engineering applications.

Examples include multicomponent flash calculation[15], equivalent continuum model construction from discrete fracture characterization[16], fracture network recognition from outcrops[17], and well data history analysis[18]. These four applications correspond to four neural networks: artificial neural network (ANN), convolutional neural network, U-Net, and long short-term memory, which are designed for value-to-value, image-to-value, image-to-image, and time series problems, respectively.

This study strives to develop a data-driven, physics featuring model based on ANN for estimating fracture permeability, with consideration of static geometric properties, e.g., mean aperture, minimum aperture, roughness, tortuosity, etc., and dynamic flow parameters, e.g., Reynolds number. Specifically, a value-to-value model is established to capture the nonlinear relationship between these static geometric and dynamic flow properties as input, and fracture permeability as output. In this study, high-resolution simulations for NS equations based on Latin Hypercube Sampling (LHS) are used to generate the data sets.

Herein, ANN coupled with Bayesian optimization is implemented to obtain the optimized surrogate model with accuracy exceeding 90% for both training and validation sets. We further test the developed surrogate model with newly generated fracture cases with a broad range of roughness and tortuosity under different Reynolds numbers. We also test its performance with the reference solutions from NS equations.

This work introduces an integrated workflow for developing a data-driven, physics included model using machine learning to estimate fracture permeability under complex physics, e.g., inertial effect. To our knowledge, this technique is introduced for the first time. The proposed model offers an efficient and accurate alternative to the traditional upscaling methods that can be readily implemented in reservoir characterization and modeling workflows.

Global Sensitivity Analysis

We can conclude from the Literature Review that the permeability of rock fractures is a complex function of some static geometric properties, e.g., mean aperture, roughness, and tortuosity, and other dynamic flow properties, e.g., Reynolds number. These traditional models, however, ignore the effect of minimum aperture. As the minimum aperture mainly controls the fluid flow within rock fractures for 2D fracture cases, its influence on fracture permeability should be considered.

In this section, global sensitivity analysis is implemented to explore the importance of these static and dynamic parameters on the model response — fracture permeability. For the generality of describing 2D rock fractures, we summarized the following five parameters as the model input parameters, including four dimensionless parameters as follows:

1. Mean Aperture: $\langle a \rangle$
2. Relative Roughness: Defined as the ratio of mean to standard deviations of aperture field[5]:

$$Relative\ Roughness = \frac{\langle a \rangle}{\sigma_a} \quad (1)$$

3. Tortuosity: Defined as the ratio of flow path distance to fracture straight-line distance[19]:

$$\tau = \frac{d_{flow-path}}{d_{straight-line}} \quad (2)$$

4. λ: Defined as the ratio of minimum to mean apertures:

$$\lambda = \frac{a_{min}}{\langle a \rangle} \quad (3)$$

5. Reynolds number: Defined as the ratio of inertial forces to viscous forces[20]:

$$Re = \frac{\rho Q}{\mu w} = \frac{\rho U \langle a \rangle}{\mu} \quad (4)$$

where ρ is the fluid density, Q is the flow rate through rock fractures, μ is the fluid viscosity, w is the fracture width, and U is the characteristic velocity choosing as the averaged mean velocity. The w is set to be 1 m for 2D fracture cases.

We perform global sensitivity analysis based on Sobol or variance-based decomposition to determine the impact of these five parameters on fracture permeability (refer to Saltelli et al. (2010)[21] for further mathematic formulation). The ranges of these uncertain parameters are collected based on the open-source data set with 7,680 2D fractures[3] and the work of Zimmerman et al. (2004)[20].

UQLab[22] is used to conduct the sensitivity analysis with 1 million realizations, which is proven to be stable. We observe in Fig. 1 that relative roughness shows the most significant influence on the fracture permeability, followed by the ratio of minimum to mean apertures, mean aperture, Reynolds number, and tortuosity. Meanwhile, we demonstrate the non-ignorable impact from the ratio of

Fig. 1 *The first-order sensitivity analysis indices using UQLab.*

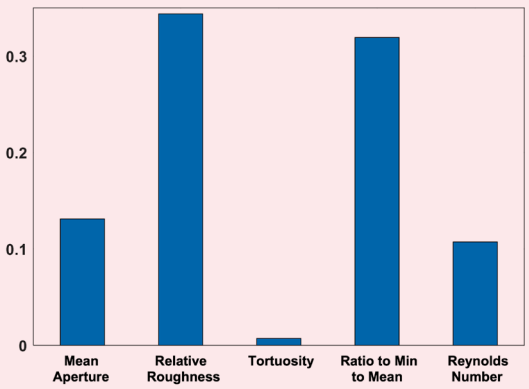

minimum to mean apertures on the permeability of 2D rock fractures. All reviewed models from the literature, however, neglect its influence on fracture permeability, making their applicabilities questionable.

Proposed Workflow

The objective of this section is to develop a data-driven, physics featuring model based on ANN for estimating fracture permeability, with consideration of static geometric properties, e.g., mean aperture, minimum aperture, roughness, tortuosity, etc., and dynamic flow parameters, e.g., Reynolds number.

Figure 2 illustrates the proposed workflow. A detailed description is presented as follows.

STEP 1: Identify Uncertain Parameters and Perform LHS

We first identify the uncertainty parameters that affect the fracture permeability. As previously mentioned, the following five uncertain parameters show a non-ignorable influence on the fracture permeability. We summarized these five significant parameters (heavy hitters) and their corresponding ranges in Table 1.

Herein, we assume uniform distributions and independent relations for all these uncertain parameters. We then generate n realizations of samples, including training and validation, using LHS theory[23] to guarantee the space filling manner. Figure 3 shows the LHS from uniform distribution (discrete design) with the different number of realizations.

STEP 2: Perform NS Simulations and Collect Inputs and Outputs from Simulations

In this step, high-fidelity simulations with parallel computing for the NS equations are run for each of the generated samples. These NS equations are solved under the mixed finite element (FE) framework, which is known for approximating the velocity fields accurately[24]. A detailed explanation of the mixed FE implementation of the NS equations is provided in Appendix A. We then collect the inputs (five uncertain parameters) and outputs (fracture permeabilities) from the simulations.

Figure 4 shows the normalized velocity field and streamline profiles obtained from the high-resolution NS simulations. We observe in Fig. 4 that an eddy occurs around places with local large asperity of the sharp corner with a high Reynolds number regimen. These eddies exert a significant influence on fluid flow through rock fractures by shrinking the effective flow channel.

The specific procedure of calculating fracture permeability based on NS solutions is detailed as follows.

- Flow rate calculation: Integrating the velocity across

Fig. 2 *The workflow for the development of the data-driven, physics featuring model.*

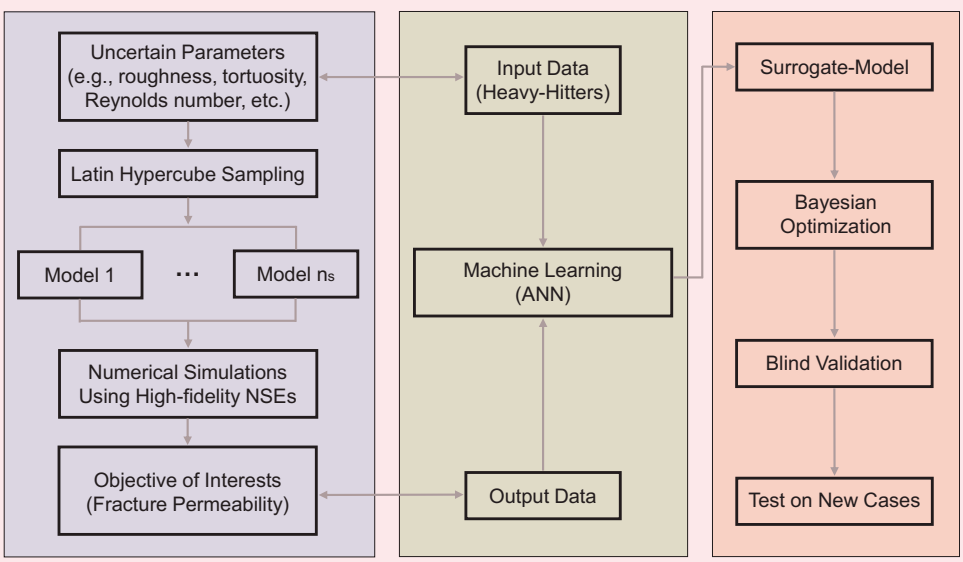

Table 1 *Uncertain parameters used in this study and their corresponding ranges.*

Uncertain Parameters	Lower Bound	Upper Bound	Distribution
Mean aperture (mm)	1.11	1.29	Uniform
Relative roughness (-)	2.23	6.96	Uniform
Tortuosity (-)	1.01	1.34	Uniform
Ratio of minimum to mean apertures (-)	0.08	0.67	Uniform
Reynolds number (-)	0.1 (Laminar flow)	100 (Nonlinear flow)	Uniform

Fig. 3 *The LHS with different numbers of realizations: (a) 50, (b) 100, (c) 300, and (d) 500. For illustration purposes, we take relative roughness vs. tortuosity as an example. As observed, the space filling trend has become more obvious with the increase of realizations.*

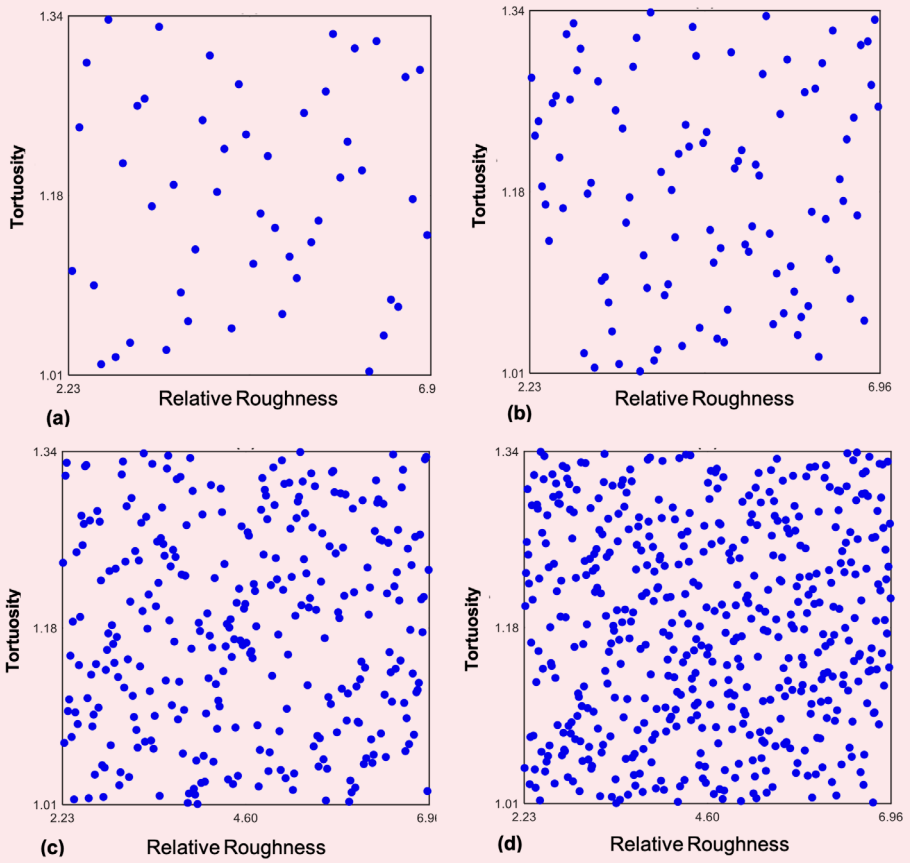

the fracture outlet leads to flow rate (denoted as Q_{NS}).

$$Q_{NS} = \int_0^w \int_0^a \left(\overrightarrow{u_{outlet}} \cdot \vec{n}\right) dwda \quad (5)$$

where w and a are the fracture width and aperture, respectively; $\overrightarrow{u_{outlet}}$ is the velocity at the outlet; and $\vec{n}$ is the unit vector normal to the outlet. The w is set to be 1 m for 2D fracture cases.

- Fracture permeability calculation: Combined Darcy's law with CL, fracture permeability (denoted as K_f) is computed as:

$$a_h = \left(\frac{12 Q_{NS} \mu}{w \nabla P}\right)^{1/3} \quad (6)$$

$$K_f = \frac{a_h^2}{12} = (12)^{1/3} \left(\frac{Q_{NS} \mu}{w \nabla P}\right)^{2/3} \quad (7)$$

where a_h is the effective hydraulic aperture, and ∇P is the pressure gradient across the flow direction.

Fig. 4 *The high-resolution NS solutions with normalized velocity field and streamline profiles under high Reynolds number with non-ignorable inertial effect.*

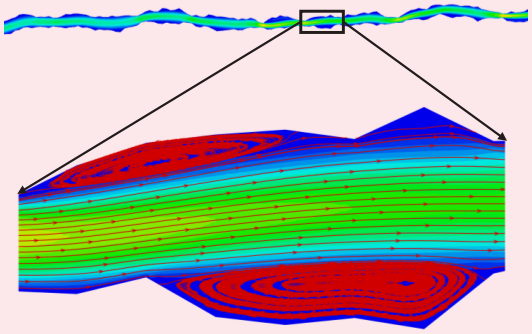

STEP 3: Construct Optimized Data-Driven Surrogate Model

This step strives to establish an optimized data-driven surrogate to map the nonlinear relationship between the inputs and outputs collected from step 2. We automate the process of tuning the hyperparameters for ANN using the Bayesian optimization algorithm instead of the manual trial-and-error tuning process. Bayesian optimization attempts to find the global optimum in a minimum number of steps. A detailed description of Bayesian optimization could be found in Brochu et al. (2010)[25].

Figure 5 illustrates the structure implemented in this work, including input layers, hidden layers, and output layers. A detailed introduction of ANN could be found in Goodfellow et al. (2016)[26].

STEP 4: Validate the Developed Surrogate Model

We conduct blind validation on the optimized data-driven surrogate model. We should pay attention to its performance on the validation samples, as the overfitting cases often occur with good predictions for training samples, yet poor predictions for validation samples. In this study, the optimization process is conducted until the accuracy exceeding 90% for both training and validation samples is reached.

The following parameters are used to assess the performance of the developed ANN model.

1. APE: The average of prediction errors, *PE*, between the predicted (denoted by $K_f^{predict}$) and ground truth (K_f^{truth}) fracture permeability.

$$PE = \left| \frac{K_f^{predict} - K_f^{truth}}{K_f^{truth}} \right| \times 100\% \quad (8)$$

$$APE = \frac{1}{N} \sum_{i=1}^{N} PE_i \quad (9)$$

2. PPE: The percentage of *PE* within an acceptable error margin — 10% is the threshold in this study.

$$PPE = \frac{N_{(where, PE \le 10\%)}}{N} * 100\% \quad (10)$$

We further test the developed surrogate model with 500 newly generated fracture cases with a broad range of roughness and tortuosity under different Reynolds numbers. In this study, inputs and outputs collected from the 500 simulations (corresponding to Fig. 3d) are fed to the ANN model for the coupling training validation process.

We summarized the optimum ANN architecture, optimum hyperparameters, and the related model evaluation

Fig. 5 *The ANN structure used in this study, consisting of three types of layers: input, hidden, and output layers. The Bayesian optimization is employed to obtain the optimum hyperparameters.*

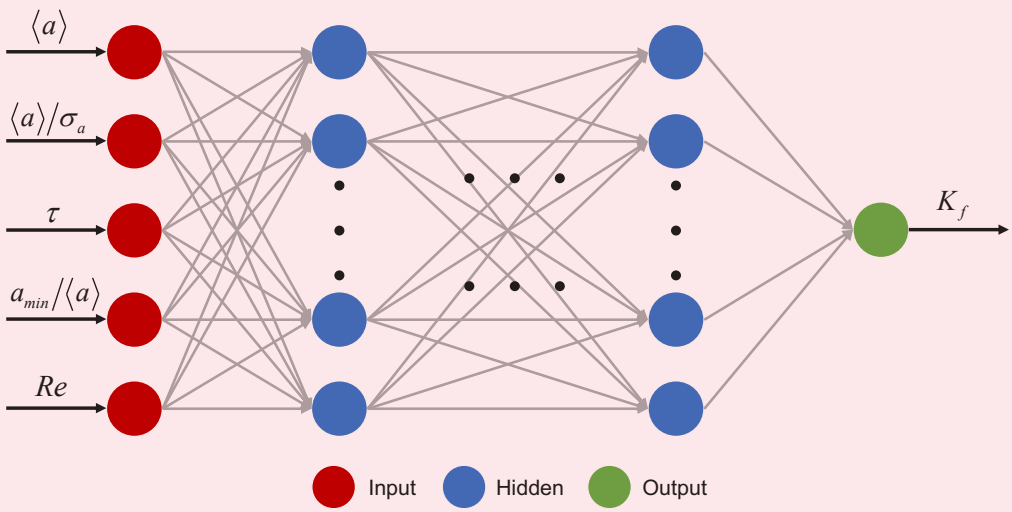

Table 2 *The optimum ANN structure, ANN hyperparameters, and model evaluation performance.*

ANN Architecture	[5 6 4] Three hidden layers with 5, 6, and 4 neurons, respectively.	
Model Training	Training Samples	400 (80%)
	APE	3.1%
	PPE	96.3%
Model Validation	Validation Samples	100 (20%)
	APE	3.5%
	PPE	97%
Model Test (Newly generated cases)	Test Samples	500
	APE	3.9%
	PPE	94.2%

performance in Table 2.

Results and Discussions

As shown in Table 2, the Bayesian optimized ANN structure exhibits the three hidden layer layout with 5, 6, and 4 neurons in each layer, respectively. We should pay attention to the overfitting issue during the coupling training validation test process. As a result, we should evaluate the overall model performance not only on training samples. The developed data-driven surrogate model reaches an accuracy exceeding 90% for all training, validation, and test samples with the corresponding values of 96.3%, 97%, and 94.2%, respectively.

Figure 6 shows the effect of epochs on the training accuracy and predictability (validation and test) of the model. We observed that the training accuracy increases, i.e., error decreases, as the number of epochs increases. The model predictability in terms of validation and test processes shows an optimum at Epoch 6, before which it's underfitting and after overfitting.

Figure 7 shows the diagonal plots between the ground truth, i.e., the reference NS, and the predicted solutions regarding fracture permeability for training (400), validation (100), test (500), and all 1,000 samples, respectively. The predicted values fall into the black diagonal lines, indicating an exact match with the reference NS solutions, while the off-diagonal values exhibit deviations. The off-diagonal points are equally distributed on each side of the diagonal lines, indicating stable performance even with complex fracture cases. The developed surrogate model performs well with the APE of 3.1%, 3.5%, 3.9%, and 3.6%, respectively.

Figure 8 shows the distributions of errors between the ground truth and predicted values, indicating that the error sizes are normally distributed. Most errors are near the zero line, with a few errors far from that. The nature of essentially normal distribution with a narrow range makes the ANN model more robust for real applications.

Fig. 6 *The effect of epochs on the training accuracy and predictability of the model.*

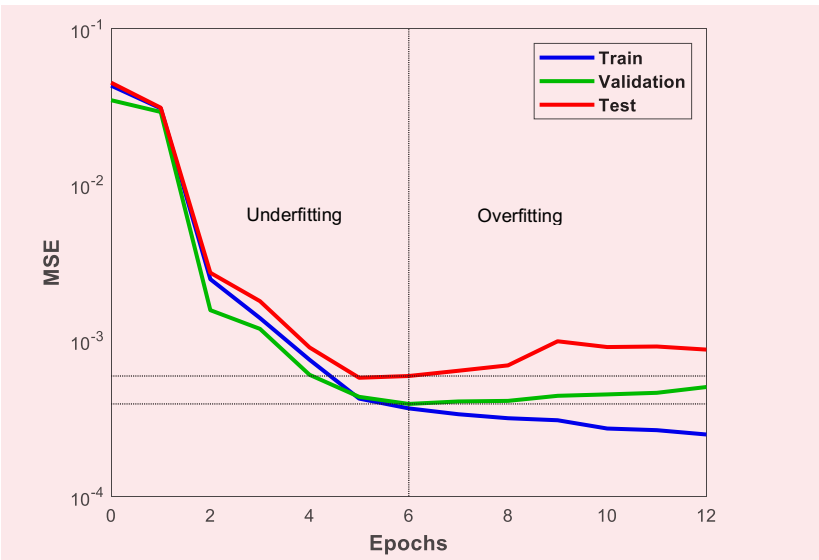

Conclusions

This study develops a data-driven, physics featuring model based on ANN for estimating fracture permeability, with consideration of static geometric properties, e.g., mean aperture, relative roughness, tortuosity, and ratio of minimum to mean apertures, and dynamic flow parameters, e.g., Reynolds number. Specifically, a value-to-value model is established to capture the nonlinear relationship between these static geometric and dynamic flow properties as input and fracture permeability as output. The proposed model offers an efficient and accurate alternative to the traditional upscaling methods that can be readily implemented in reservoir characterization and modeling workflows.

The main conclusions are summarized as:

Fig. 7 *The diagonal plots show the ground truth and predicted fracture permeabilities for: (a) training, (b) validation, (c) test, and (d) all samples.*

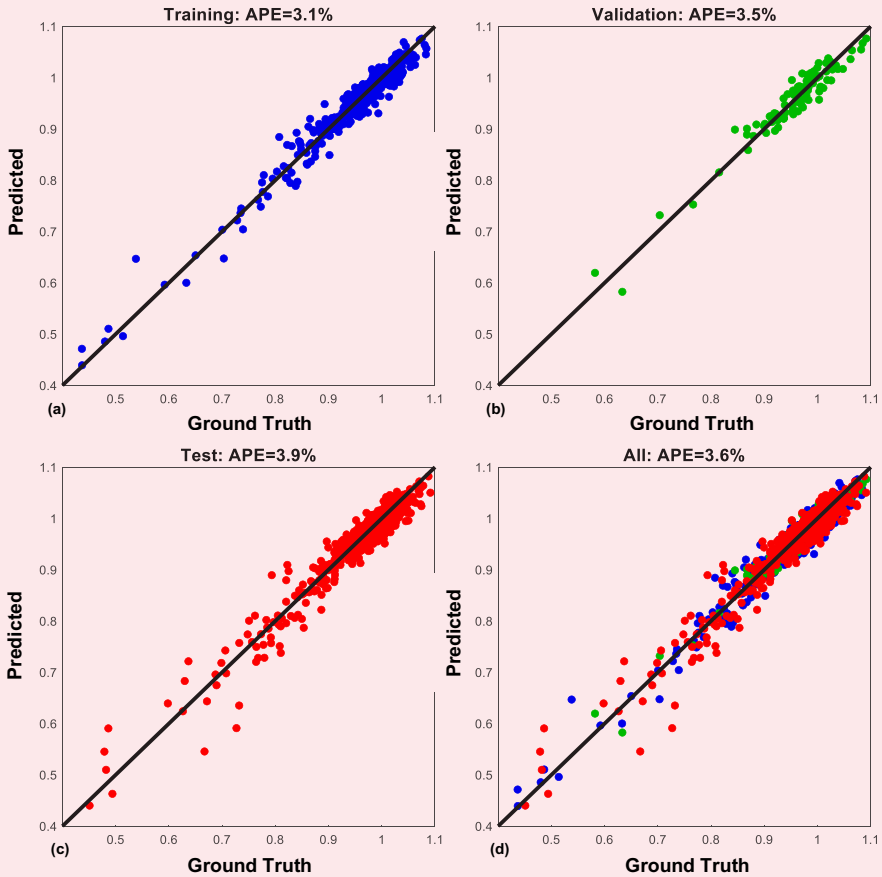

- ANN could be successfully implemented as an efficient and accurate tool to estimate the permeability of rock fractures as an alternative to traditional analytical approaches.
- Global sensitivity analysis based on Sobol or variance-based decomposition is performed to explore the impact of these five static and dynamic properties on fracture permeability. Results show that except for roughness, tortuosity, and inertia (represented by Reynolds number), the ratio of minimum to mean apertures exerts a non-ignorable influence on the permeability of 2D rock fractures. All reviewed models from the literature, however, neglect its effect on fracture permeability, making their applicabilities questionable.
- The quality of training/validation/test samples significantly affects the quality of the ANN-based surrogate model and further its applicability. In this work, high-resolution NS simulations coupled with parallel computing techniques are used to generate the data sets.
- The space filling manner using the LHS technique guarantees the quality of the developed surrogate by using minimum data sets.

Fig. 8 *A histogram showing the distributions of errors. Herein, positive values indicate overestimation, while negative ones correspond to underestimation.*

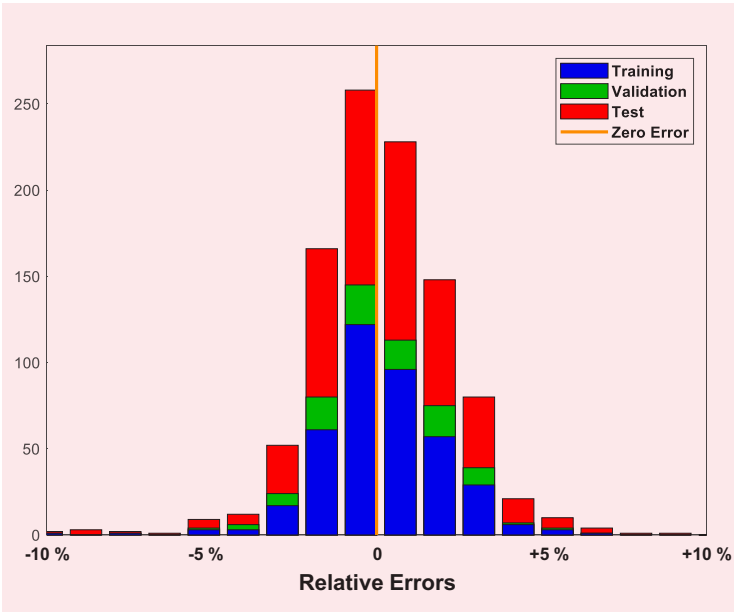

- The Bayesian optimization algorithm provides an efficient approach for determining the network structure and tuning related hyperparameters instead of the manual trial-and-error process.
- The developed surrogate model changes from underfitting to overfitting status as the number of epochs increases. We should avoid the overfitting issue by evaluating the overall model performance on the training/validation/test samples.
- The proposed surrogate model achieves an accuracy exceeding 90% for all training/validation/test samples, demonstrating its broad applicability and robustness and readiness for real application.
- We should pay attention to the gradient vanishing issues when dealing with deep neural networks.

The focus of the work is to develop an ANN-based, big data-driven, and physics featuring model for 2D rock fractures. Future work could be extended to include more complex topics, such as pressure and velocity fields estimation, and an extension to 3D cases.

Appendix A: Mixed Finite Element Formulation

Consider the steady-state of incompressible, Newtonian laminar flow with no gravity effects, and the full physics NS equations can be given as:

$$\rho\left(\vec{u}\bullet\nabla\vec{u}\right)=-\nabla p+\mu\nabla^2\vec{u}$$
$$\nabla\bullet\vec{u}=0 \qquad A1$$

In Eqn. A1, $\vec{u}$ is the velocity vector, ρ is the density, p is pressure, and μ is viscosity.

We assume no-slip boundary conditions to the walls of the fracture, and pressure values are set at the fracture's outlet and inlet, Fig. A1. The gradient of velocity in the direction of the pressure gradient is set to zero to guarantee the fully developed flow and to avoid the inlet effect.

The NS equations can be formulated in a mixed variational form, where the pressure, and the velocity, are simultaneously approximated. Multiplying Eqn. A1 by a test function, $(\vec{v},q)$, and integrating the resulting equations over the domain Ω yields:

$$\int_\Omega\rho\left(\vec{u}\bullet\nabla\vec{u}\right)\bullet\vec{v}dx=\int_\Omega\left(-\nabla p\right)\bullet\vec{v}dx+\int_\Omega\left(\mu\nabla^2\vec{u}\right)\bullet\vec{v}dx$$
$$\int_\Omega\left(\nabla\bullet\vec{u}\right)qdx=0 \qquad A2$$

Applying the integration by parts technique, we have:

$$\int_\Omega\left(-\nabla p\right)\bullet\vec{v}dx=\int_\Omega p\nabla\bullet\vec{v}dx-\int_{\partial\Omega}p\vec{v}\bullet\vec{n}ds$$
$$\int_\Omega\left(\mu\nabla^2\vec{u}\right)\bullet\vec{v}dx=-\mu\int_\Omega\nabla\vec{u}:\nabla\vec{v}dx+\mu\int_{\partial\Omega}\nabla\vec{u}\bullet\vec{n}\vec{v}ds \qquad A3$$

The problem becomes, find $\left(\vec{u},p\right)\in W$, such that,

$$a\left(\left(\vec{u},p\right),\left(\vec{v},q\right)\right)=L\left(\left(\vec{v},q\right)\right) \qquad A4$$

where $\left(\vec{v},q\right)\in W$, and

$$a\left(\left(\vec{u},p\right),\left(\vec{v},q\right)\right)=\rho\int_\Omega\left(\vec{u}\bullet\nabla\vec{u}\right)\bullet\vec{v}dx-$$
$$\int_\Omega p\nabla\bullet\vec{v}dx+\mu\int_\Omega\nabla\vec{u}:\nabla\vec{v}dx+\int_\Omega\left(\nabla\bullet\vec{u}\right)qdx \qquad A5$$

$$L\left(\left(\vec{v},q\right)\right)=-\int_{\partial\Omega_N}p_{inlet}\vec{v}\bullet\vec{n}ds-\int_{\partial\Omega_N}p_{outlet}\vec{v}\bullet\vec{n}ds \qquad A6$$

In Eqn. A6, $W=V\times Q$ is a mixed function space such that for $q\in Q$ and $\vec{u}\in V$.

Acknowledgments

We would like to thank Saudi Aramco for funding this research. We would also like to thank King Abdullah University of Science and Technology (KAUST) for providing a license of MATLAB.

This article was presented at the SPE Annual Technical Conference and Exhibition, Dubai, UAE, September 21-23, 2021.

References

1. He, X., Hoteit, H., AlSinan, M.M. and Kwak, H.T.: "Modeling Hydraulic Response of Rock Fractures under Effective Normal Stress," paper presented at the ARMA/DGS/SEG International Geomechanics Symposium, virtual, November 3-5, 2020.
2. Brush, D.J. and Thomson, N.R.: "Fluid Flow in Synthetic Rough-Walled Fractures: Navier-Stokes, Stokes, and Local

Fig. A1 *An illustration of the boundary conditions imposed on a rough walled fracture.*

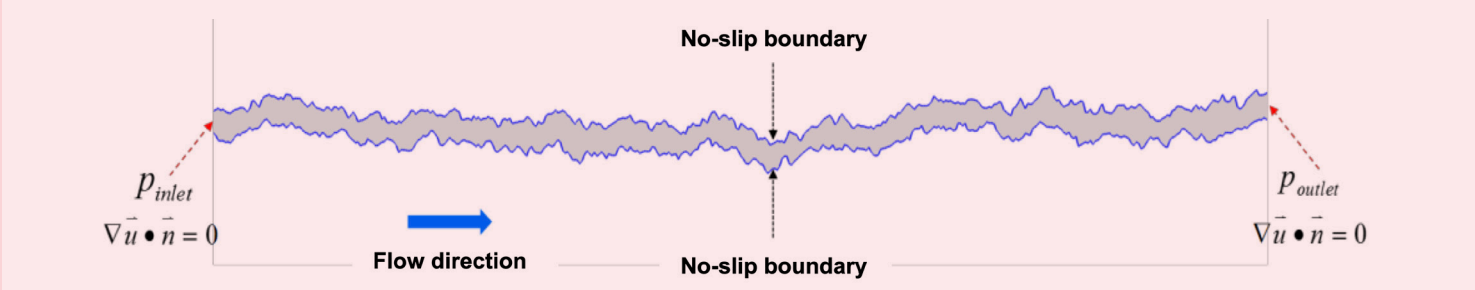

Cubic Law Simulations," *Water Resources Research*, Vol. 39, Issue 4, April 2003.

3. He, X., AlSinan, M.M., Kwak, H.T. and Hoteit, H.: "A Corrected Cubic Law for Single-Phase Laminar Flow through Rough-Walled Fractures," *Advances in Water Resources*, Vol. 154, August 2021.

4. Snow, D.T.: "Anisotropie Permeability of Fractured Media," *Water Resources Research*, Vol. 5, Issue 6, December 1969, pp. 1273-1289.

5. Brown, S.R.: "Fluid Flow through Rock Joints: The Effect of Surface Roughness," *Journal of Geophysical Research*, Vol. 92, Issue B2, February 1987, pp. 1337-1347.

6. Renshaw, C.E.: "On the Relationship between Mechanical and Hydraulic Apertures in Rough-Walled Fractures," *Journal of Geophysical Research*, Vol. 100, Issue B12, December 1995, pp. 24629-24636.

7. Unger, A.J.A. and Mase, C.W.: "Numerical Study of the Hydromechanical Behavior of Two Rough Fracture Surfaces in Contact," *Water Resources Research*, Vol. 29, Issue 7, July 1993, pp. 2101-2114.

8. Amadei, B. and Illangasekare, T.: "A Mathematical Model for Flow and Solute Transport in Non-Homogeneous Rock Fractures," *International Journal of Rock Mechanics and Mining Sciences & Geomechanics Abstracts*, Vol. 31, Issue 6, December 1994, pp. 719-731.

9. Lomize, G.M.: "Water Flow through Jointed Rock (in Russian)," Gosenergoizdat, Moscow, 1951.

10. Louis, C.: "A Study of Groundwater Flow in Jointed Rock and Its Influence on Stability of Rock Masses," in *Rock Mechanics Research Report/Imperial College of Science and Technology*, Vol. 10, 1969, 90 p.

11. Patir, N. and Cheng, H.S.: "An Average Flow Model for Determining Effects of Three-Dimensional Roughness on Partial Hydrodynamic Lubrication," *Journal of Lubrication Technology*, Vol. 100, Issue 1, January 1978, pp. 12-17.

12. Zimmerman, R.W. and Bodvarsson, G.S.: "Hydraulic Conductivity of Rock Fractures," *Transport in Porous Media*, Vol. 23, April 1996, pp. 1-30.

13. Wang, Z., Xu, C. and Dowd, P.: "A Modified Cubic Law for Single-Phase Saturated Laminar Flow in Rough Rock Fractures," *International Journal of Rock Mechanics and Mining Sciences*, Vol. 103, March 2018, pp. 107-115.

14. Xiong, X., Li, B., Jiang, Y., Koyama, T., et al.: "Experimental and Numerical Study of the Geometrical and Hydraulic Characteristics of a Single Rock Fracture during Shear," *International Journal of Rock Mechanics and Mining Sciences*, Vol. 48, Issue 8, December 2011, pp. 1292-1302.

15. Zhang, T., Li, Y., Li, Y., Sun, S., et al.: "A Self-Adaptive Deep Learning Algorithm for Accelerating Multicomponent Flash Calculation," *Computer Methods in Applied Mechanics and Engineering*, Vol. 369, September 2020.

16. He, X., Santoso, R. and Hoteit, H.: "Application of Machine Learning to Construct Equivalent Continuum Models from High-Resolution Discrete Fracture Models," IPTC paper 20040, presented at the International Petroleum Technology Conference, Dhahran, Kingdom of Saudi Arabia, January 13-15, 2020.

17. Santoso, R., He, X. and Hoteit, H.: "Application of Machine Learning to Construct Simulation Models from High-Resolution Fractured Formation," SPE paper 197439, presented at the Abu Dhabi International Petroleum Exhibition and Conference, Abu Dhabi, UAE, November 11-14, 2019.

18. Li, Y., Sun, R. and Horne, R.: "Deep Learning for Well Data History Analysis," SPE paper 196011, presented at the SPE Annual Technical Conference and Exhibition, Calgary, Alberta, Canada, September 30-October 2, 2019.

19. Walsh, J.B. and Brace, W.F.: "The Effect of Pressure on Porosity and the Transport Properties of Rock," *Journal of Geophysical Research*, Vol. 89, Issue B11, October 1984, pp. 9425-9431.

20. Zimmerman, R.W., Al-Yaarubi, A., Pain, C.C. and Grattoni, C.A.: "Nonlinear Regimes of Fluid Flow in Rock Fractures," *International Journal of Rock Mechanics and Mining Sciences*, Vol. 41, Supplement 1, May 2004, pp. 163-169.

21. Saltelli, A., Annoni, P., Azzini, I., Campolongo, F., et al.: "Variance-Based Sensitivity Analysis of Model Output. Design and Estimator for the Total Sensitivity Index," *Computer Physics Communications*, Vol. 181, Issue 2, February 2010, pp. 259-270.

22. Marelli, S. and Sudret, B.: "UQLab: A Framework for Uncertainty Quantification in Matlab," paper presented at the 2nd International Conference on Vulnerability and Risk Analysis and Management and the 6th International Symposium on Uncertainty, Modeling, and Analysis, Liverpool, U.K., July 13-16, 2014.

23. Santoso, R., Torrealba, V. and Hoteit, H.: "Investigation of an Improved Polymer Flooding Scheme by Compositionally Tuned Slugs," *Processes*, Vol. 8, Issue 2, 2020, pp. 197-216.

24. Hoteit, H. and Firoozabadi, A.: "An Efficient Numerical Model for Incompressible Two-Phase Flow in Fractured Media," *Advances in Water Resources*, Vol. 31, Issue 6, June 2008, pp. 891-905.

25. Brochu, E., Cora, V.M. and de Freitas, N.: "A Tutorial on Bayesian Optimization of Expensive Cost Functions, with Application to Active User Modeling and Hierarchical Reinforcement Learning," *http://arxiv.org/abs/1012.2599*, 2010.

26. Goodfellow, I., Bengio, Y. and Courville, A.: *Deep Learning*, Cambridge: MIT Press, 2016, 775 p.

About the Authors

Xupeng He

M.S. in Petroleum Engineering, King Abdullah University of Science and Technology

Xupeng He is currently a Ph.D. student at the Ali I. Al-Naimi Petroleum Engineering Research Center, King Abdullah University of Science and Technology (KAUST), Thuwal, Saudi Arabia. His research interests include modeling naturally fractured reservoirs, machine (deep) learning applications in petroleum engineering, and uncertainty quantification and optimization in subsurface flow problems.

Xupeng is the author of 11 conference papers, and two U.S. patents.

He was the recipient of the Excellent Student Cadre and the Outstanding Undergraduate Student Awards in 2014 and 2015, respectively, at Chang'an University. Also, Xupeng received a national scholarship from the Ministry of Education of the People's Republic of China in 2012 and 2013.

He received his B.S. degree in Resource Exploration Engineering (Oil and Gas) from Chang'an University, Xi'an, China, in 2015. Xupeng received his M.S. degree in Petroleum Engineering from KAUST in 2018.

Marwah M. AlSinan

M.S. in Petroleum Engineering, Imperial College

Marwah M. AlSinan joined Saudi Aramco in 2013 as a Petroleum Engineer, working with the Reservoir Engineering Technology Division in the Exploration and Petroleum Engineering Center – Advanced Research Center (EXPEC ARC).

Her research interests include multiphase flow in fractures, carbon dioxide sequestration, and applications of nuclear magnetic resonance in porous media.

In 2013, Marwah received her B.S. degree in Petroleum and Natural Gas Engineering from Pennsylvania State University, State College, PA. She received her M.S. degree in Petroleum Engineering from Imperial College, London, U.K. in 2017.

Dr. Hyung T. Kwak

Ph.D. in Physical Chemistry, Ohio State University

Dr. Hyung T. Kwak joined Saudi Aramco in April 2010 as a Petroleum Engineer with Saudi Aramco's Exploration and Petroleum Engineering Center – Advanced Research Center (EXPEC ARC). He had been a member of the Pore Scale Physics focus area and the SmartWater Flooding focus area of the Reservoir Engineering Technology Division. Since 2014, Hyung has been a focus area champion of the Pore Scale Physics focus area. His main research focus is seeking a deeper understanding of fluid-rock interaction in pore scale of the Kingdom's reservoirs.

Since joining Saudi Aramco, Hyung has been involved with various improved oil recovery and enhanced oil recovery (EOR) research projects, such as SmartWater Flooding, carbon dioxide EOR, and chemical EOR. Currently, he is leading a suite of key EXPEC ARC Fourth Industrial Revolution technology projects. Prior to joining Saudi Aramco, Hyung was a Research Scientist at Baker Hughes, from 2001 to 2010, focused on research related to nuclear magnetic resonance (NMR)/magnetic resonance imaging technology.

In 1996, Hyung received his B.S. degree in Chemistry from the University of Pittsburgh, Pittsburgh, PA, and in 2001, he received his Ph.D. degree in Physical Chemistry from Ohio State University, Columbus, OH.

Before moving into the oil and gas industry, Hyung was involved — as a postdoctoral fellow for 2 years — in a project developing the world's largest wide bore superconducting magnet NMR spectrometer, 900 MHz, at the National High Magnetic Field Laboratory.

He has more than 300 publications, including peer-reviewed articles and patents.

Dr. Hussein Hoteit

Ph.D. in Applied Mathematics, University of Rennes 1

Dr. Hussein Hoteit is an Associate Professor in Reservoir Engineering and the Program Chair of Energy Resources and Petroleum Engineering (ERPE) at King Abdullah University of Science and Technology (KAUST), Thuwal, Saudi Arabia.

Before joining KAUST, Hussein worked for ConocoPhillips and Chevron Companies for about 12 years, where he conducted projects related to chemical enhanced oil recovery (EOR), CO_2 EOR, steam flood, EM heating, to name a few.

Hussein's current research includes chemical EOR, geological CO_2 storage, improved oil recovery optimization, data-driven machine learning, and reservoir simulation development.

He has earned several Society of Petroleum Engineers (SPE) awards, including SPE Distinguished Lecturer in 2009, and served as Associate Editor for the *SPE Journal* for more than 10 years.

Hussein received his B.S. degree in Pure Mathematics and Computer Sciences from Lebanese University, Lebanon, M.S. and Ph.D. degrees in Applied Mathematics from the University of Rennes 1, Rennes, France.

Electric Submersible Pump Design Enhancements for H_2S Harsh Environments

Mohammed A. Al-Khalifah, Rui F. Pessoa and Derek M. Sinclair

Abstract /

The electric submersible pump (ESP) remains the preferred artificial lift method for high rate production when technically viable. ESPs, on the other hand, are sensitive to downhole conditions and pumped fluid. Sour fields, in particular, are considered a major challenge for producing facilities and well completion elements. Reservoirs producing fluids with hydrogen sulfide (H_2S) present a special challenge to ESP systems.

This article utilizes ESP field observations and pulled equipment findings from many dismantled inspection and failure analyses (DIFA). The findings confirmed H_2S behavior and root causes of electrical and mechanical failures within multiple ESP components. The outcome of these investigations and the recommended system upgrades to enhance its reliability in a corrosive environment will be illustrated.

Critical ESP system materials will deteriorate and fail when subjected to sour environments. H_2S can penetrate the ESP cable insulation, attack the copper, and react to form copper sulfide (Cu_2S) resulting in electrical failure. It can also permeate the seal bags and O-rings, diffuse in the seal's dielectric oil, and attack the bronze and copper components in the seal and the motor. To improve reliability, a new version of the motor lead extension (MLE), using three individually armored connectors and a seal with a H_2S sacrificial anode scavenger inside each chamber were introduced. The improved design encapsulated the insulated conductors individually within metal tubes made of high nickel alloy. The tubes can be terminated individually at the motor and above the production packer with proven swage type connectors.

By utilizing high nickel alloy tubes as barriers against H_2S and removing all connections below the packer, the H_2S effect has been eliminated. On the other hand, the seal with a H_2S passive scavenger will retain most of the H_2S in the dielectric oil before it reaches the motor. These novelty technologies enhanced the ESP's reliability and prolonged its run life, resulting in significant well intervention savings and increased well availability.

Introduction

Sour well environments provide a unique set of challenges for electric submersible pumping (ESP) systems to overcome, and also provide the robustness and run lives as delivered in sweeter wells. Market solutions for sour well ESP products at the time were not delivering expected average run lives and suffering from repeated and similar failure mechanisms. Hydrogen sulfide (H_2S) was penetrating ESP sealing mechanisms and barriers intended to protect the ESP systems from H_2S attack, resulting in a reduction in the ESP's run life.

Three common areas of H_2S ingress were identified during the dismantled inspection and failure analyses (DIFAs), namely the motor lead extension (MLE), the electrical connectors/penetrators, and the seal/protector component located between the ESP motor and pump. H_2S would then react with subcomponents, such as copper conductors to form copper sulfide (Cu_2S), which deteriorated electrical insulating barriers leading to a lower than expected run life.

Solutions were initiated, particularly for these three areas and new components; materials and procedures were developed to improve the robustness, and consequently, the run lives of the ESP systems in sour environments.

ESP Completions

The ESP completion for the majority of the studied wells consists of a downhole multi-sensor, motor, tandem seal sections, centrifugal pump, MLE, Y-tool, hydraulically set packer with packer electric penetrator, round power cable to surface, tubing, subsurface safety valve, wellhead tubing hanger, wellhead penetrator, and wellhead tree.

Figure 1 shows the well schematic for a typical ESP completion utilized for sour fields. The ESP packer is typically located 200 ft above the pump to isolate the tubing annulus and protect the main cable from the sour environment, which is located directly below the packer.

The ESP is a standard configuration of the motor, seal/protector, and pump with a Y-tool to allow intervention access below the ESP. The ESP motor is connected to the main cable run via an MLE cable that has a pothead connection into the motor, a lead barrier over the 200 ft of cable to prevent H_2S ingress and an electrical penetrator

to ensure pressure integrity at the packer. The seal/protector allows for expansion of the dielectric motor oil while ensuring produced fluids do not enter the motor and lead to failures.

The major subcomponents of the ESP system found to suffer attack from H_2S were the ESP packer penetrator, the MLE cable, the motor pothead, and the seal/protector section.

H_2S Challenges

Throughout all DIFAs conducted, the extent of damage to the ESP components was found, but no root cause of failure. The severity of the damage was seen to be directly proportional to the H_2S partial pressure[1] of the reservoir from which the ESP was producing. The higher the partial pressure of H_2S, the more corrosion was found on components, e.g., the power cable, MLE, seal bushings, and bearings.

Although the initial failure rate was small, the commonality of damage by H_2S attack required further action. The ESP run life was being degraded due to early failure of the MLE component, the motor pothead, and the packer penetrator. Failures would occur due to microcracking of the lead barrier allowing H_2S ingress and consequent pitting corrosion of the electrical copper conductors. A product improvement plan was initiated to tackle the issues encountered and protect or isolate said ESP components from future H_2S ingress.

DIFA of Failed ESP Systems

ESP run life is a very important factor for producers using this method of artificial lift. It is expected that the target run days go far beyond the vendor's warranty. Excellence in ESP performance are part of the goals pursued by oil field operators to maintain the lowest possible lifting costs. With this in mind, all ESPs that do not reach the target run life are dismantled and exhaustive failure analysis is carried out to capitalize on the lessons learned and identify areas of ESP improvement or technology development if needed.

Some ESP systems that exhibit good run life, mostly in excess of 10+ years, are dismantled and analyzed too. So, the information presented here is based on real observations and evidence collected during the DIFA process for ESP equipment, particularly components that didn't reach the target run days.

Failures on the MLE and Pothead

The MLEs widely used since the sanctioning of most sour field developments requiring ESP have been either the plug-in or tape-in pothead type with a standard monobore connection to the motor. Stringent internal standard requirements called for high temperature grade, harsh environment, and the highest electrical rating of 5 kV. MLE with a lead sheath protecting the conductors' insulation, Monel wrapped armor and pothead back filling with epoxy and/or lead have being successfully used, in many cases with run lives exceeding 10 years.

Nevertheless, weaknesses related with cracks in the lead sheath have resulted in many failures. These cracks allowed H_2S to attack the copper conductors, mainly near where the lead jacket terminated into the pothead body or at the interface between the MLE cable and the pothead. Figure 2 shows examples of a tape-in and plug-in type pothead.

Traditionally, a lead jacketed MLE cable has been used in the belief that lead kept out well fluids. Lead is a recognized impermeable material, even for gases. A good number of motor lead cables that checked bad electrically were dismantled to show damage to the lead jacket, which allowed H_2S ingress and conductor corrosion. The origin of these cracks has been identified from manufacturing due to excessive armor tightening, handling in the field during installation, or the presence of contaminants in the lead. The lesson learned is that the lead sheath cannot be trusted as an effective barrier.

Fig. 1 *A typical ESP completion.*

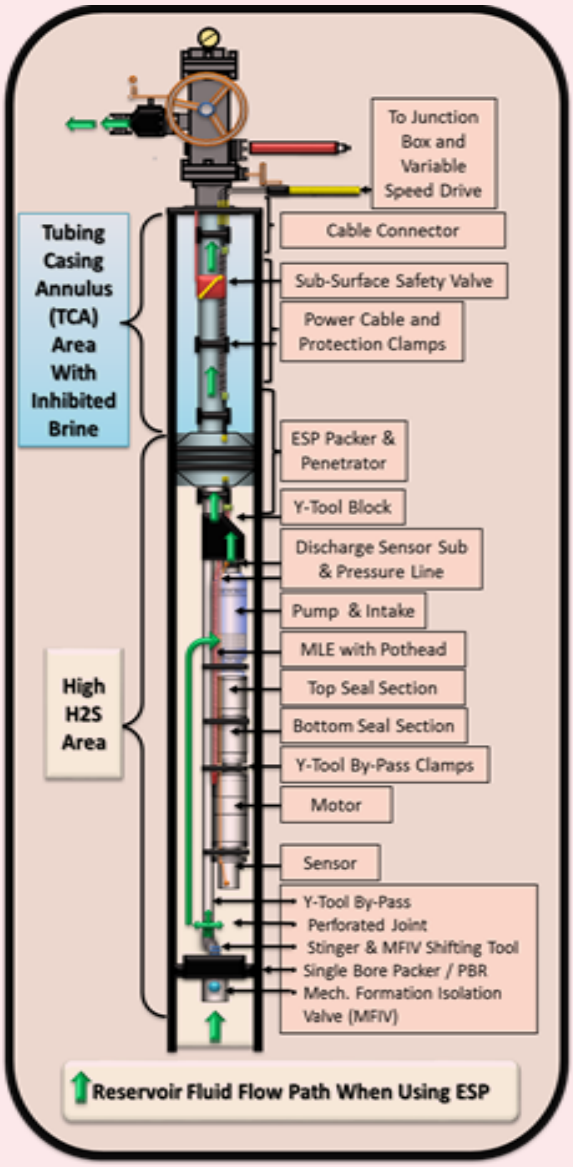

Fig. 2 *Examples of the common area of an MLE pothead failure due to H_2S attack.*

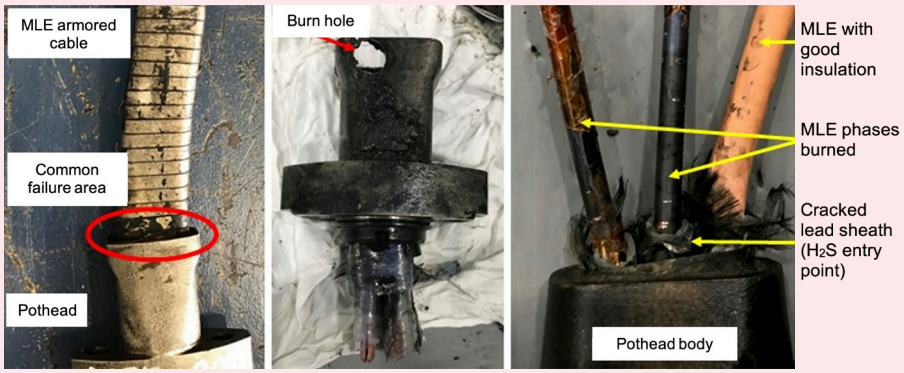

From the DIFA evidences, once the H_2S infiltrates through the lead sheath, it permeates the secondary cable insulation, usually made of ethylene-propylene-diene-monomer (EPDM) rubber. It also starts breaching the overlap wrapped polyimide film that commonly forms the primary insulation, usually through the easiest path, which is the interstices of the film. In contact with the conductor, the H_2S corrodes the copper wire, leading to Cu_2S buildup as a byproduct. This mechanism creates the characteristic pattern, Fig. 3. The MLE finally fails, either because the wire cross section is reduced by corrosion and cannot continue supporting the electrical load, or because the Cu_2S grows enough to breakdown the insulation.

A good improvement in the traditional H_2S MLE with a regular pothead connection was achieved by upgrading the insulation from EPDM and polyimide (Kapton®) to polyether ether ketone (PEEK). It is believed that the low permeation rate of H_2S through PEEK, coupled with the very tight conformance of the insulation to the conductor, poses a stronger barrier for H_2S to reach the copper conductors.

Although improved QA/QC plans, periodic manufacturing inspection, field service audits and new insulation materials allowed a generous improvement in reducing the failure rates, the standard harsh environment MLEs with a monobore pothead continued being a risk in achieving long run lives consistently in wells with high partial pressures of H_2S. A game changer technology to overcome this challenge has been the metal-to-metal sealing MLE, whose details are presented later.

Failures on Penetrators and Electrical Connectors

The common well completion practices in harsh fields require a packer above the ESP. This well barrier provides enhanced well control for safety purposes and protects the casing from corrosive fluids like H_2S and carbon dioxide. On the other hand, it requires the use of an electrical penetration system to communicate the ESP power cable and the MLE.

Penetrators are also required to pass through the tubing hanger and the wellhead in the surface (wellhead

Fig. 3 *H_2S corrosion of an MLE copper wire under EPDM secondary insulation and polyimide primary insulation due to a cracked lead sheath.*

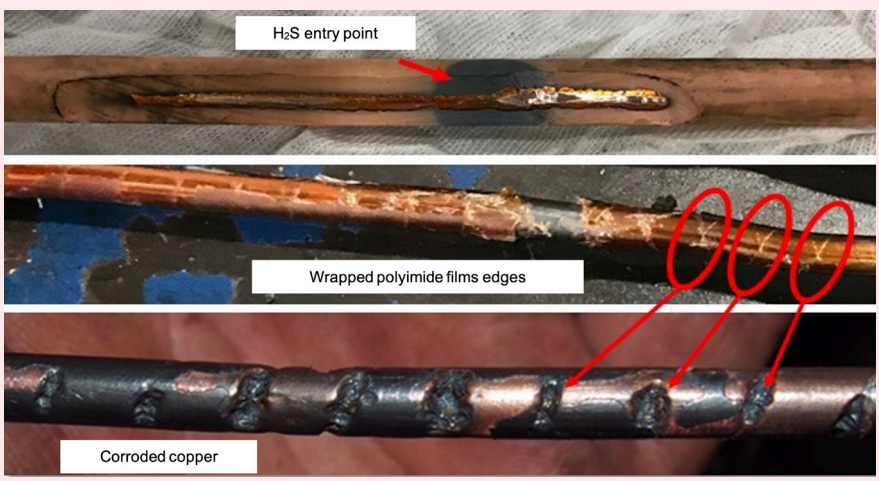

penetrators).

The design of both packer and wellhead penetrators share several commonalities based on its function of pressure containment but the exposure to different operational conditions and corrosiveness of the environment makes them inherently different, so it is their relative failure rate. Historically, the packer penetrators have shown a higher number of failures, many of them likewise to MLEs, a consequence of H_2S corrosion on the lower connectors — below the ESP packer. In fact, the failures associated to the penetrators were a bigger concern since these triple the MLE cases.

All electrical penetrator manufacturers rely on some type of elastomeric seal to isolate the electrical connections from the well fluids. The more common materials are Aflas and hydrogenated-nitrile-butadiene rubber, which have a high permeation rate to H_2S. The penetrator connectors tend to fail within one to three years, depending on H_2S partial pressure. Both factory molded and field attachable penetrators have been used in harsh environments. Although the factory molded pieces have shown slightly better performance, they have not been widely accepted mainly due to the hassles related with longer manufacturing lead times, bigger reels for shipping and handling, and longer rig times due to accurate space out required between the packer and the ESP motor.

The packer's penetrator lower connectors have consistently been a major failure component in high H_2S partial pressure fields. Initially, many tear downs were done in the original equipment manufacturer's factory and formal reports were prepared and delivered to the ESP contractor. The reports were consistent in their conclusions even though little analysis was actually done. Many recurrent findings were therefore misdiagnosed and attributed to the wrong root causes.

One cause of failure was assigned as "explosive decompression" of the connector, Fig. 4; however, deeper analysis demonstrated that it was actually a mechanical failure as the corrosion was so severe that the Cu_2S byproduct grew so large that the steel tube could not withstand the pressure[2].

This has been confirmed on many other penetrators where the Cu_2S bumps are in early growing stages, Fig. 5.

Another cause of failure was attributed to decompression leak of boot seals, Fig. 6, but this type of failure could never be repeated in laboratory testing. The productivity indices of these wells are generally very high so there is no production scenario that could give cause to a rapid drop in pressure below the packer. The low-pressure drops have been repeatedly evidenced by direct measurement through the ESP downhole sensor or permanent downhole monitoring gauges available in some completions.

Figure 7 shows another common finding in many penetrators, which either failed or are still with good electrical readings. Staining and carbon-like deposits in the electrical connectors were attributed to high heat. Deeper evaluation and lab analysis proved that this diagnosis was wrong as it turned out to be deposits of Cu_2S — effects of crevice H_2S corrosion. Despite that

Fig. 4 *A burst in a penetrator tube due to excessive pressure exerted by the growth of the copper corrosion byproduct.*

Fig. 5 *The Cu_2S bumps growing under the PFA cable insulation inside a penetrator capillary tube.*

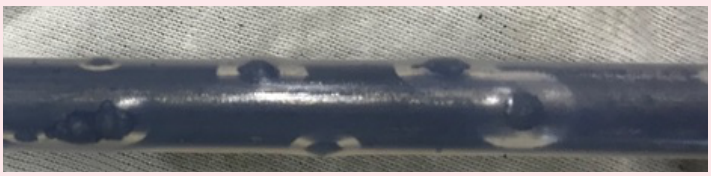

Fig. 6 *The suspected decompression failure of a boot seal.*

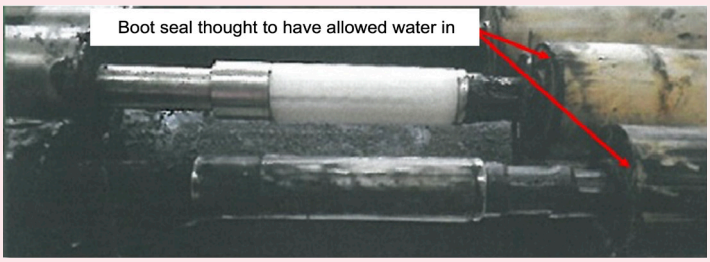

Fig. 7 *The suspected heat effect (top) turned out to be H_2S corrosion (bottom).*

the connectors are gold plated, the gold layer is damaged during the crimping process, exposing bare copper that is then attacked by H_2S.

Another usual finding in some failed penetrators has been an insulation burn inside the lower connector capillary tubes, Fig. 8. In general, the root cause of this issue has been attributed to poor electrical power quality by penetrator manufacturers without any solid fundamentals. Even penetrators that had good insulation readings (megging) were found to have problems that could only be seen during the dismantle stage. For example, the penetrator components in Fig. 9 would not have been dismantled based on the good insulation, but they have given some of the strongest evidence yet of what the true root cause of failure is.

In the case of perfluoroalkoxy (PFA) insulated cable, e.g., Figs. 8 and 9, H_2S finds micro-voids underneath the insulation. As the corrosion moves further away from the H_2S entry point, it becomes progressively worse as the pH in the micro environments within the crevices becomes more acidic. The Kapton® insulated motor lead cable previously shown in Fig. 2 appears to be very different, and yet the root cause of failure is the same, it is crevice corrosion from an H_2S attack.

Since Cu_2S is a semiconductor in most of its forms, the insulation, once damaged, can cause electrical treeing[3], Fig. 10, for a cable pulled from a sour field. Despite this condition being concerning, the electrical insulation megged good during the dismantling process, however, a complete premature insulation breakdown should be expected at any point soon.

Failures on ESP Seals (Protectors)

ESP seals, also known as protectors, play a very important role in the reliability and run life of the ESP system. A vast majority of wells require that the pumping system be installed at inclinations that require the use of bag chambers for appropriate isolation of the motor oil from the well fluids. This way the standardized ESP string design includes dual tandem seals with a minimum of two bag chambers on each, and all connected in a series for maximum redundancy. Parallel configuration of the bags is rarely required. For sour environments, good recommended practices and internal standards call for an Aflas elastomer throughout the seal assembly, which includes the bags, the O-rings, and the boot sealing elastomer of the shaft mechanical seals.

The experience from the DIFAs is that the H_2S can permeate the elastomers reaching up to the motor regardless of the number of redundant chambers and that bags are not broken. Nevertheless, a higher number of redundant chambers will delay the process. The invasion of H_2S progresses from top to bottom, which is evident from the decreasing damage in terms of corrosion and staining of parts in the same direction. Some parts in the seal that are traditionally made of bronze or aluminum bronze like the radial bearings, thrust rings, thrust bearings, and recirculation oil pumps, will suffer some degree of corrosion despite the fact that they are fully wetted by dielectric oil. This is because the H_2S dissolves in the dielectric oil as it permeates through the bags.

Fig. 8 *Insulation burn attributed to poor power quality.*

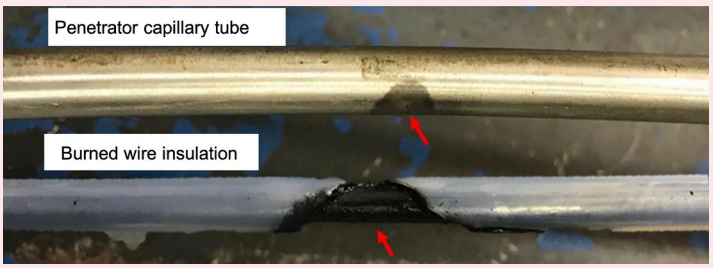

Fig. 9 *Cu_2S encroachment in PFA insulation (megger reading 501 GΩ).*

Fig. 10 *Electrical treeing in a cable with good electrical readings.*

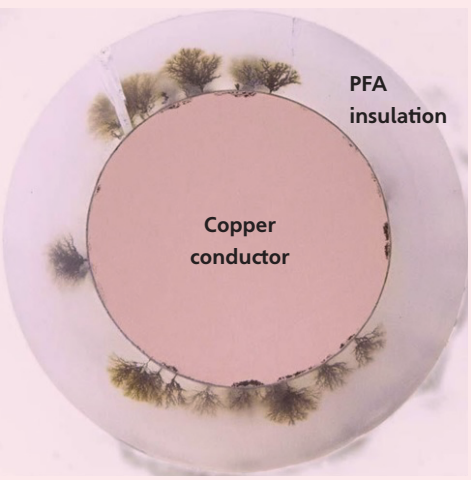

Figure 11 shows an example of highly corroded bearings and a recirculation oil pump. It can be observed the considerable material lost to corrosion and growing Cu_2S. The effects of debris in the dielectric oil and the lack of bearings lubrication are catastrophic as these cascade into major problems such as well fluid contamination to the motor or shaft snapping.

Even the highest strength shafts of nickel alloy 718 used

Fig. 11 *H_2S corroded seal bronze parts vs. original.*

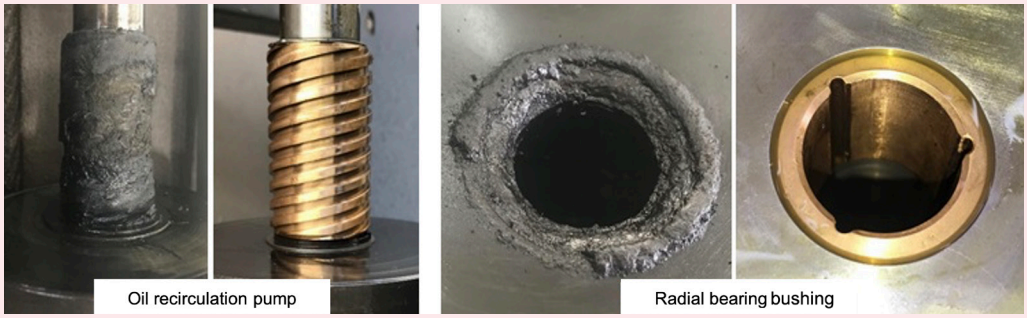

Fig. 12 *The effects of corroded bronze bushings in seal shafts.*

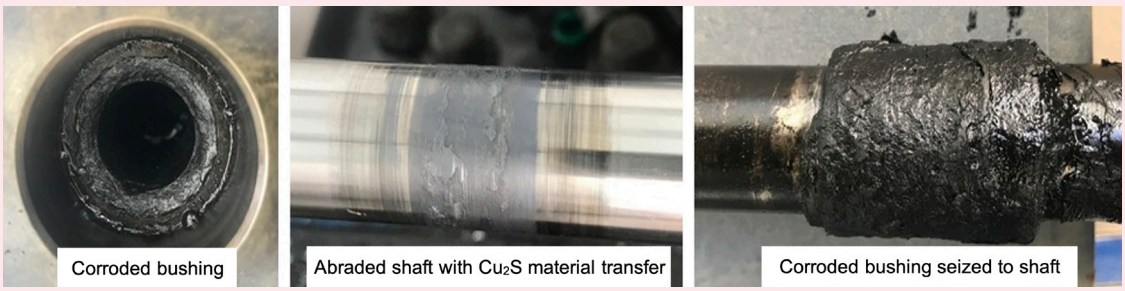

in ESP equipment can succumb to the lack of lubricity and material transfer from corroded bronze bushings, Fig. 12. The process starts with localized heat, abrasion of the shaft and material transfer of the growing Cu_2S byproduct until the shaft either snaps or the bushings become seized to the shaft and start spinning with it leading to higher vibration and temperature.

As concluded from these DIFA evidences and discussed in some published literature for harsh environments, the recommendation is to use seals with compliant radial bearings (journal type) of hardened material throughout the seal assembly. Either cermets like tungsten carbide or ceramics like silicon carbide or zirconia are commonly used. Many installed seals have included these only in the seal head and/or the seal base while bronze bearings are still used in the seal guides in between. This will certainly affect the reliability of the ESP system sooner or later depending on the H_2S partial pressure and the bronze composition.

The bronze composition is a very important variable when dealing with H_2S. Some solid bronze casting parts such as thrust rings and fixed pad design thrust bearings are commonly found stained black due to superficial H_2S corrosion, but without concerning material loss or growing deposits of Cu_2S when used as upthrust bearings. This type of bronze has some aluminum content — aluminum bronze alloy — and can survive in sour environments depending on the load conditions, even with the presence of moisture. This is attributed to the pacifying properties of aluminum oxide films[4] and the low removal rate of such films considering the limited and intermittent load carried by the ESP seal in the upthrust bearings. Based on these DIFA evidences and the risks of fluttering tilting pad bearings used as upthrust carriers, a vast majority of the seals installed in a sour environment are not completely "bronze free." These still rely on either a ring or bearing of aluminum bronze to handle upthrust loads.

For downthrust load carrying purposes the preferred bearings have been of the tilting pad design with polymer lining. These are more tolerant to misalignment and have the ability to accommodate a considerably wider range of loads and speeds. The only issue observed with these in sour environments is that the manufacturers typically use a substrate of bronze between the carbon steel bearing carriers and the lining polymer to improve the bonding of the polymer. The substrate is attacked by H_2S and the lining polymer is found many times delaminated from the carrier, Fig. 13.

Based on the observations of many DIFAs and the summarized findings presented, it has been possible to identify opportunities of improvement through the development of new seal technology. A periodic review of internal Engineering Standards is performed to ensure these are updated according to lessons learned, best recommended practices and always reflect the state-of-the-art in ESP knowhow for harsh environments.

Fig. 13 *The delamination of lining polymer in tilting pad thrust bearings initiated by H_2S corrosion of the bronze substrate.*

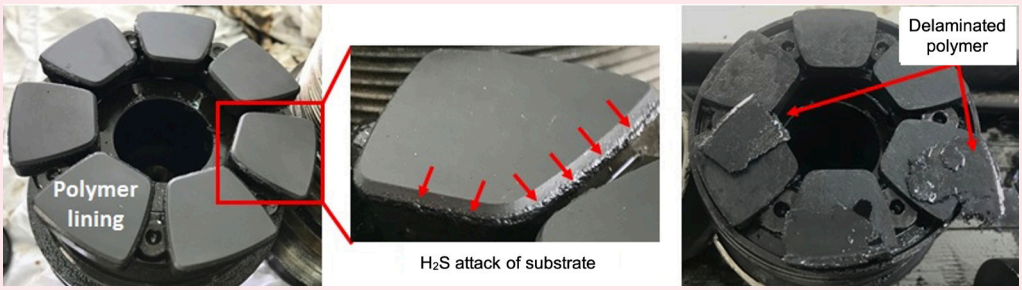

Product Improvements

In this section, we will explain the product improvements for the previous three major challenges in equipment reliability in sour wells.

MLE Improvement

The need for an MLE consistently more reliable in harsh environments has been the drive for novel ideas. The objective was to develop a new MLE minimizing if not avoiding the use of elastomers and/or epoxy directly exposed to well fluid and thereby at risk of H_2S penetration.

Initial developments focused on improving the insulation of the MLE copper wires with materials less permeable to H_2S in an effort to prevent the findings discussed previously. This first step in the learning curve had good success incorporating PEEK to replace EPDM and wrapped Kapton®. Like in the former MLE, a lead sheath was used as the barrier to keep H_2S away of the PEEK insulation. This improved version was still limited using elastomer sealing on the pothead to motor connection, therefore posing a risk for H_2S to enter the system.

A drawback of this MLE was that the greater hardness and stiffness of the PEEK insulation increased the risk of damaging the lead sheath by the outer armor. Furthermore, the arrangement of all three MLE phases entering together in the classic pothead creates a challenging geometry to seal. Since this model was still having the three cable phases armored together and a monobore motor pothead, a second step in the learning curve was splitting the phases. A new version[5], Fig. 14, was then introduced with the following features and benefits:

- The three MLE phases were split, armored independently and connected separately in the motor head. This facilitated the individual sealing of each conductor within its motor connector when compared with the classic monobore pothead. This is because there is more space available for the operators to perform the soldering operation required for sealing.
- Three individual armored connectors are better protected from mechanical damage while running in the well.
- Less prone to human error, considering the simple connection when compared with tape-in MLE pothead.

Fig. 14 *The first version of split phase MLE.*

- Each motor connector has pressure test ports to verify integrity during installation, which has been a previous failure mode.
- The manufacturer's qualification was performed up to 45% H_2S at 3,000 psi and 425 °F, which far exceeded the partial pressures in the field.

Although this improvement was another great achievement in the learning curve, it did not address all the concerns identified for a harsh environment. The sealing system of the connectors, now substantially reduced in terms of exposed area to well fluids, was still based in elastomers even though these were upgraded from Aflas to Chemraz 562. It also still needed the use of packer penetrator lower connectors (below the ESP packer), which were identified as a possible entry point of H_2S in the electrical system from many DIFA findings. Actually, the penetrator was the failed component in a field trial test of this MLE carried in a sour well. The MLE itself was found to be good, but it ended up not being well accepted as harsh environment technology due to these weaknesses and the penetrator failure as part of

the overall ESP system.

One ESP vendor proposed an alternative MLE with split phases and metal-to-metal sealing from the back of the pothead up to above the packer by simple adaptation of an existing two piece subsea pothead — also used in extreme temperature steam assisted gravity drainage wells. The connection of this pothead to the motor was still of monobore geometry, similar to the classic pothead. Likewise, the main seal with the motor is an elastomer boot and a lead gasket. Another lead gasket was used to seal in between the two pieces of the pothead body. Both lead gaskets promised at least some "soft" metal-to-metal sealing around the motor head. This was an attractive alternative when compared with the other available MLE technologies for some of the wells with the highest H_2S partial pressure. Therefore, multiple wells were fitted with ESPs using this MLE pothead technology. Figure 15 is a photo of two variants of this pothead with angled and straight tubes.

Although this alternative had a good rate of success it still showed some weaknesses:

- Lead again was not the most reliable sealing material due to the difficulty to keep an even compression between the pothead body parts in the field.
- Stiffness of the tubes in relation to the short distance these penetrate in the back compression fittings.
- The pothead is not pressure testable after made up to the motor.

The first two weaknesses increased the risk of failing the metal seals either due to rough handling during installation or when running in the well. Therefore, this MLE technology was susceptible of well fluid leakage either through the back fittings or any of the lead gaskets and require improvement. These causes were confirmed after a few premature failures, although the average run life still doubled that for the classic harsh environment MLE.

The MLE development learning curve continued following multiple trial tests. A reliable metal-to-metal sealing technology was developed to seal the MLE from the motor head to above the ESP packer[6]. Figure 16 shows three different types from three different suppliers of the full metal-to-metal sealing MLEs from the motor up to above the packer.

This technology encapsulates each of the three electrical conductors on individual metal tubes. Resistant metallurgy to H_2S such as nickel alloy or nickel-copper alloy is used in the tubes that extend from the motor connector up to the top of the ESP packer, eliminating the need for a packer penetrator. Metal-to-metal sealing at the motor is achieved through compression swage type ferrules or C-rings directly in the motor head ports or a fit for purpose head adapter. The tubes pass through the ESP packer where they are sealed using metal-to-metal compression fittings. In the tubing-casing annulus (TCA), above the packer, electrical connectors provide electrical continuity between the MLE conductors and the ESP power cable for each separate phase. The MLE tubes are terminated with metal-to-metal standard compression fittings coupled to the electrical connectors' housing.

Fig. 15 *The former models of pothead applied for harsh environment.*

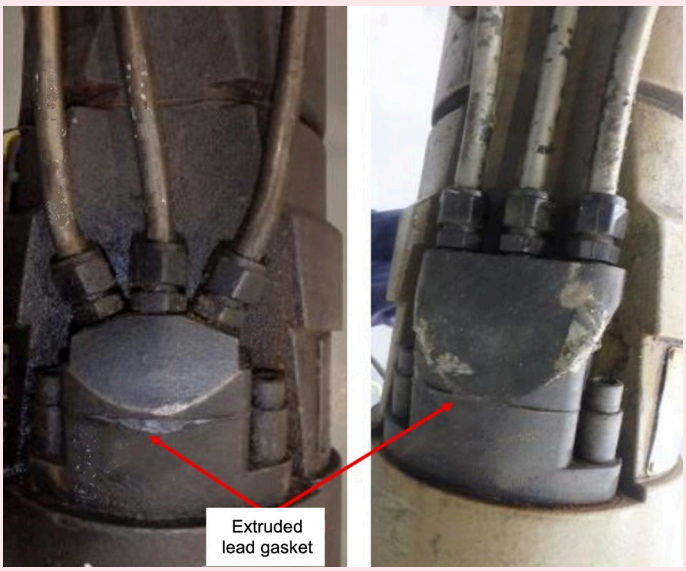

Fig. 16 *Three different MLEs with metal-to-metal sealing technology.*

Packer Penetrators Improvements

The field attachable packer penetrator's — with connectors below the packer — recent improvements positively impacted the reliability in harsh environments. Nevertheless, this technology lost relevance for the wells with higher partial pressure of H_2S after the introduction of the full metal-to-metal sealed MLE.

One improvement of the older penetrators included changing the penetrator wire insulation material from PFA to PEEK and increasing its thickness. Another improvement was doubling the thickness of the gold plating over the electrical terminals and switching to a crimping process less aggressive to minimize the risk of damaging the gold plating layer. Additionally, a layer of PEEK tape was wrapped over the crimped zone until the end of the penetrator tube in an attempt to avoid H_2S entering any crevices between parts. These and other minor changes have significantly increased reliability and reduced the penetrators' failure rate. The penetrators run time expectancy was extended but the H_2S permeation problem has not been completely solved. Subsequently, the field attachable penetrators remain useful and more cost-effective for mild harsh environments.

On the other hand, a reliable electrical connector is still required for terminating the metal-to-metal MLE tubing with the round cable (main cable) in the TCA above the packer. The design conditions are challenging since the connectors have to sustain the TCA completion fluid hydrostatic column, the testing pressure of the packer and the pressure cycles related to TCA fluid thermal expansion. Accordingly, a stringent procedure is required for the electrical connector or splice tube qualification. For the subject case, the electrical connectors were tested with 50 pressure cycles between 1,500 psi to 6,500 psi along with five thermal cycles simultaneously. All test samples were required to pass the current leakage criteria and the DIFA inspection after testing. Following this procedure led to a reliable system with an extended run life.

ESP Seals Improvement

The three main improvements performed in the seals that have proven very successful were:

- Extend the use of hardened compliant radial bearings throughout the seal (previously used only in heads and bases).
- Standardizing Aflas as the material for the bags and O-rings exposed to well fluid.
- Implementation of copper sacrificial anodes inside the chambers as a H_2S scavenger.

The implementation of copper as a H_2S scavenger is perhaps the most novel approach in developing a seal for high H_2S partial pressures. For this purpose, a static sleeve of copper is fitted concentric to the guide tube inside each bag (B) and/or labyrinth (L) depending on the chamber type. After the H_2S permeates through the elastomer bag, it dissolves into the dielectric oil and is then sequestered by the copper sleeve, which progressively corrodes forming Cu_2S as a byproduct. There was some concern about this technique due to contamination of the oil with Cu_2S and the release of large amounts of debris, but experience has proven that it works.

Most of the corrosion byproduct remains attached to the copper sleeve so no significant amount of debris are released, which is different than when H_2S attacks parts under relative motion like the radial bronze bushings or the downthrust bearing. Additionally, the top chambers capture the greater percentage of H_2S easing the exposure of the lower chambers.

Figure 17 shows a copper sleeve exposed after cutting the bag in the lower chamber of a lower dual tandem seal (six total chambers configured in a series as L/B/B-B/B/B from top to bottom) and the oil from the same chamber. This well failed due to a pump problem after 909 days of operating. The oil was very clean and had a dielectric strength of 21 kV.

Figure 18 shows a comparison of the H_2S scavenger copper sleeves for an upper tandem seal configured with three bags in a series (B/B/B). This ESP ran for 332 days in a sour well and was pulled without failure. It can be observed how the top copper scavenger is highly corroded compared with others. The center scavenger

Fig. 17 *Dielectric oil and H_2S scavenger from the lowest bag in a severe service ESP seal.*

(middle seal's chamber) has some minor corrosion since most H_2S was scavenged in the top bag. Finally, just a very low concentration of H_2S reaches the lower seal chamber, so the copper scavenger is just superficially stained. For this well, the scavengers fitted in the lower tandem seal bags were corrosion free (copper retained its original color).

Another improvement to the ESP seal for a harsh environment was the implementation of shaft mechanical seals with a metal bellow, Fig. 19, instead of an elastomer boot. Although it can be used throughout the seal assembly, it is required for the top chamber at least.

One more improvement that is currently ready for field-testing is the use of metal below to replace the elastomer bag in the seal's top two chambers. The implementation of metal bellow technology in both the top shaft mechanical seal and the top chambers has two objectives:

- Maximize the reliability of the top chambers as the ESP seal's first barrier through which the H_2S has to pass.
- Significantly reduce the elastomer area exposed to H_2S to minimize its permeation to the lower ESP seal.

Other efforts and developments ongoing are to completely replace a few bronze parts that remain in the seal like the upthrust ring and the downthust bearings with tilting pads that use bronze to improve the lining polymer bonding. These have not been a major threat to achieve long run lives in sour H_2S wells, however, the goal is to strive to consistently extended the ESP run life to 10+ years.

Summary of Improvements

Table 1 summarizes the improvements discussed and others in general of the ESP string for severe H_2S service.

Conclusions

The partial pressure of H_2S is a good indicator to the severity of the environment where standard ESP systems are utilized for wells containing H_2S. Acceptable run lives can be delivered for lower partial pressure wells, however, the common failure modes will occur at some point in the ESP's lifetime.

Isolation of the MLE cable from the well environment by using nickel-copper alloy tubing has proven to prevent H_2S ingress, which the lead barrier cable could not repeatedly deliver. The metal tubes provide an effective barrier to H_2S throughout the cable length and do not degrade or crack during installation, which was a common failure mode of lead.

Replacing the motor pothead with three individual metal compression seals has prevented H_2S ingress as seen due to failed lead and elastomer seals. Unlike standard ESPs, the connection to the motor can now be pressure tested to ensure integrity before running in the hole.

Replacing the packer penetrator for electrical connectors only above the ESP packer and allowing a metal seal around the MLE tubes has isolated it from the well environment, thereby eliminating any H_2S ingress potential through this component.

Fig. 18 *A comparison of H_2S scavengers from a B/B/B seal showing H_2S corrosion progress from upper (left) to lower (right) bag chambers.*

Fig. 19 *A comparison of shaft face mechanical seals.*

The seal/protector improvements included changing bronze materials for cermets/ceramics, upgrading Aflas bags and including sacrificial copper anodes inside the bags. These changes have shown to be effective in preventing H_2S to reach the motor.

Since the introduction of the product improvements presented here, there have been no re-occurrences of the failure mechanisms seen at the MLE and connection points to the motor or packer. The run life of ESP systems is increasing in high H_2S partial pressure wells and the failure rates are more aligned to that of the sweeter fields. The new product has become the new standard to be installed for wells where high H_2S partial pressures are encountered.

Table 1 *A summary of the improvements discussed and others in general of the ESP string for severe H_2S service.*

Item	Initial System	Improved System
O-Rings Elastomers	Highly Saturated Nitrile (HSN), Viton	Aflas
Packer Seal Material	HNBR and Nitrile	Aflas
MLE: • Insulation • H_2S barrier • Motor connection • MLE pothead to motor seal	Standard Hi-Temp (KELB): • Kapton®/EPDM Rubber • Lead sheath • Tape-in and plug-in • O-ring (HSN, Viton, Aflas) • Boot	Hi H_2S Partial Pressure Design: • PEEK, Kapton® + PFA • Inconel or Monel tube • Individual phases threaded • Metal-to-metal • EPDM rubber
Trim Material (Fasteners, drain/fill plugs)	Silicon Bronze and Carbon Steel	Monel
Packer Electric Penetrator: • Insulation • H_2S barrier	Molded Rubber: • HNBR • HNBR or Aflas	MLE tubes (metal-to-metal seal): • PEEK or Kapton® + PFA • Inconel or Monel Tube
Round power cable (In the TCA)	Non-leaded and EPDM/EPDM	Lead sheath and EPDM/EPDM
Seal Section/Protectors: • Radial bearings • Mechanical shaft seal bellows • Mineral oil reservoir bags • Mineral oil reservoir bag scavenger • Thrust bearing	B/L – B/L – HSN: • Bronze shaft bushings • Elastomer – HSN or Aflas • HSN • None • Bronze	L/B/B – B/B/B or B/B/B – B/B/B or B/B – B/B or MB/MB/L – BL/BL/L (trial): • Cermet or ceramic compliant bearings: Tungsten carbide, silicon carbide or zirconia • Inconel metal bellow • Aflas • H_2S scavenger copper sleeves • Polymer lining carbon steel

List of Abbreviations	
B	Bag type seal chamber
BL	Labyrinth in a bag seal chamber
L	Labyrinth type seal chamber
MB	Metal bellow seal chamber

References

1. Metso Automation Inc.: *Materials of Construction for NACE Applications*, Jamesbury Technical Bulletin T101-4, Issue 4/2004, 6 p.
2. Al-Khalifa, M.A., Cox, R.L. and Saad, H.: "Electric Submersible Pump Installation and Commissioning — Challenges and Lesson Learned from Field Development," SPE paper 177990, presented at the SPE Saudi Arabia Section Annual Technical Symposium and Exhibition, al-Khobar, Kingdom of Saudi Arabia, April 21-23, 2015.
3. Tabata, T., Nagai, H., Fukuda, T. and Iwata, Z.: "Sulfide Attack and Treeing of Polyethylene Insulated Cables — Cause and Prevention," paper presented at the IEEE Summer Meeting and International Symposium on High Power Testing, Portland, Oregon, July 18-23, 1971.
4. Oshe, E.K., Saakiyan, L.S. and Efremov, A.P.: "Corrosion Behavior of Aluminum Alloys in the Presence of Hydrogen Sulfide," *Protection of Metals*, Vol. 37, Issue 6, November 2001, pp. 572-574.
5. Schlumberger: *Trident — Extreme Conditions Motor Lead Extension*, brochure, 2017, 2 p.
6. Xiao, J.J., Shepler, R.A., Windiarto, Y., Parkinson, S., et al.: "Development and Field-Test of ESP Reliable Power Delivery System," SPE paper 182760, presented at the SPE Kingdom of Saudi Arabia Annual Technical Symposium and Exhibition, Dammam, Kingdom of Saudi Arabia, April 25-28, 2016.

About the Authors

Mohammed A. Al-Khalifah

M.S. in Petroleum Engineering, King Fahd University of Petroleum and Minerals

Mohammed A. Al-Khalifah is a Petroleum Engineer working in the South Khurais Production Engineering Unit of Saudi Aramco's Southern Area Production Engineering Department. He has been with Saudi Aramco since August 2006. Mohammed's experience includes work with several different departments, including Artificial Lift, Production Engineering, and Reservoir Management.

Currently, Mohammed is the Supervisor for the Onshore Artificial Lift Unit and is leading a number of projects in relation to electric submersible pump technologies and reliability.

He holds the Society of Petroleum Engineers (SPE) Petroleum Engineering certification, and the Lean Six Sigma Green Belt certification from Saudi Aramco's Organization Consulting Department.

In 2006, Mohammed received his B.S. degree in Petroleum Engineering from King Fahd University of Petroleum and Minerals (KFUPM), Dhahran, Saudi Arabia. In 2009, he received his M.S. degree in Petroleum Engineering from KFUPM, after pursuing his degree as a part-time student.

Rui F. Pessoa

M.S. in Petroleum Engineering, University of Tulsa

Rui F. Pessoa is a Petroleum Engineer Specialist working as a subject matter expert in the Technical Support Unit of the Artificial Lift Division of Saudi Aramco's Production & Facilities Development Department. He has over 28 years of experience in artificial lift, mostly dedicated to the electric submersible pumping (ESP) method. Rui started his career in 1993 as an ESP Scientist at Intevep, the R&D branch of Venezuela's National Oil Company, PDVSA. He did lab research on pump performance with free gas, high viscosity fluids, gas-liquid separators, ESP with hydro-cyclone for downhole water separation, etc. Rui also provided technical support to PDVSA operational units for all aspects related with ESP, and facilitated several courses.

He switched to the oil and gas services sector with Baker Hughes (BH) in 2005 working for the Artificial Lift Services (ALS) product line where he worked in several positions, such as Lead Application Engineer, Regional Engineer for Latin America, Project Engineer and Engineering Manager. Some of his duties included design, sizing, commissioning, optimization, troubleshooting and reliability of ESPs for a number of customers across several countries. Rui was BH's lead engineer responsible for high-end and renamed ESP subsea projects such as Shell's BC-10 Parque das Conchas and Enauta's Atlanta, and the phase 1 of Equinor's offshore development Peregrino.

Prior to joining Saudi Aramco in 2017, he was working at BH-ALS headquarters and manufacturing facility in the U.S. providing ESP technical support worldwide and end-to-end product engineering improvement.

Rui is the author/coauthor of over 20 papers on ESP.

He received his B.Eng. degree from the Universidad Central of Venezuela, Caracas, Venezuela, and his M.S. degree from the University of Tulsa, Tulsa, Oklahoma, all in Petroleum Engineering.

Derek M. Sinclair

B.Eng. in Mechanical Engineering, Glasgow University

Derek M. Sinclair is a Senior Petroleum Engineer working in the Onshore Artificial Lift Unit of Saudi Aramco's Production and Facility Development Department, where he is focused on artificial lift development and deployment. Derek has provided subject matter technical, operational, and product development support within the department with a focus on the harsh environment solutions.

Before joining Saudi Aramco in 2015, he worked for 14 years with Baker Hughes' Artificial Lift departments in various technical and project roles worldwide. Prior to this, Derek worked as a Mechanical Design Engineer.

In 1992, he received his B.Eng. degree (with honors) in Mechanical Engineering from Glasgow University, Glasgow, U.K., and following this his M.S. degree in Offshore Engineering from Robert Gordon University, Aberdeen, Scotland, U.K.

A New Oriented Perforation Strategy for Hydraulic Fracturing Treatment in Deep and Tight Reservoirs

Dr. Kaiming Xia, Dr. Yufeng Cui and Dr. Tariq Mahmood

Abstract /

Hydraulic fracture initiation can be a challenging issue for fracturing deep and tight gas reservoirs, which generally requires a high breakdown pressure for clustered perforation hydraulic fracturing treatment. Oriented perforation represents a potential solution to this issue, which cannot only lower breakdown pressure but also deliver a better oriented fracture geometry.

In this article, we present a new strategy to tackle this issue, which includes a framework to calculate the optimum perforation direction, and a new perforation cluster layout design. The optimum perforation direction is defined as the one, along which hydraulic fractures can be initiated with the lowest breakdown pressure for a perforation cluster. It can be used to control the perforation device rotating and fired in the right direction in the subsurface. Further, we present a new perforation cluster layout design, which can alleviate the near wellbore fracture tortuosity and deliver a better fracture initiation when it is aligned along the optimum perforation direction in the subsurface.

With the two parts of the strategy working together, fracture initiation from a perforation cluster can be achieved a lot easier than using the conventional perforation method. This new perforation strategy can alleviate the near wellbore fracture tortuosity, minimize fluid flow restriction and reduce pressure friction loss during hydraulic fracturing treatment. Otherwise, multiple and reoriented nonplanar fractures originated from the wellbore perforation cluster likely lead to a premature screen out, which can negatively impact fluid injection to achieve a desired stimulation performance.

Hydraulic fracturing treatment in deep and tight gas reservoirs can be improved through the following actions: calculating breakdown pressure and optimum perforation direction, using a new perforation cluster layout design, and aligning the perforation cluster in the right direction.

Introduction

Hydraulic fracture initiation in deep and tight gas reservoirs can be a challenging issue, which generally requires a high breakdown pressure. Oriented perforation can be used to alleviate the breakdown issue, which can, not only lower breakdown pressure but also deliver a better fracture geometry. The optimum perforation orientation can alleviate the near wellbore fracture tortuosity issue, minimize fluid flow restriction, and friction pressure loss during hydraulic fracturing. Otherwise, multiple and reoriented nonplanar fractures, originating from wellbore perforation clusters, may likely lead to a premature screen out and negatively impact the fluid injection potential to achieve a desired stimulation performance.

Perforating vertical or horizontal wells represent two special cases of oriented perforation, in which perforating guns can be easily oriented in the direction of maximum horizontal stress, along which hydraulic fractures will be initiated and propagated. For horizontal wells generally drilled in the minimum horizontal stress direction, hydraulic fractures will propagate toward the maximum horizontal stress direction once the fracture successfully initiates from the near wellbore.

Figure 1 shows a horizontal well drilled in the direction of minimum horizontal stress, which has three perforations. The stress regimen is the strike slip, and has $\sigma_{Hmin} < \sigma_v < \sigma_{Hmax}$. The three perforations are in the horizontal direction, vertical direction, and deviated direction. In Fig. 1, the cross sections of the perforations (red line) are plotted nearby. The horizontal perforation aligns in the direction of maximum horizontal stress. The vertical perforation is at the bottom. Perforating vertical or horizontal wells can lead to hydraulic fracture propagating in the maximum horizontal stress direction, but requires different breakdown pressure acting on the perforation tunnels. For a vertical well, the optimum perforation direction will be in the maximum horizontal stress direction, which can be easily determined. Subsequently, for a deviated, cased hole, and clustered perforation hydraulic fracturing treatment, it is relatively difficult to determine the optimum perforation direction without an analytical solution.

So far, very little work on this topic has been published in open literature; although a few articles have discussed orienting perforation[1, 2], which mainly focused on sand control. None of them has given any concrete procedures or formulations to calculate the optimum perforation direction. For this reason, this article provides an analytical approach to calculate the optimum perforation direction, which can be applicable to a deviated, cased hole, and

clustered perforation hydraulic fracturing treatment.

In this article, the optimum perforation direction is defined as the one along which hydraulic fractures can be initiated with the lowest breakdown pressure for a perforation cluster in a subsurface geologic setting. The method to determine the lowest breakdown pressure for a deviated, cased hole, and clustered perforation has been presented[3], which can account for the casing-cement-rock interaction effect, perforation quality, and stochastic properties. The details on this work can be found in a patent[3] and will not be repeated in this article. Based on the lowest breakdown pressure and its corresponding phase angle predicted by the model[3], the oriented perforation azimuth and perforation dip can be subsequently calculated.

In this article, the formations for this part will be specifically discussed and presented. The optimum perforation orientation — perforation angle, perforation azimuth, and perforation dip — can be used to control the perforation device rotated so that the charged gun can be fired in the right direction for a subsurface geologic setting. This can ensure that the perforation cluster has perforations aligning in the optimum direction and needs the minimum breakdown pressure for fracture initiation. This can improve the success rate of the hydraulic fracturing treatment in deep and tight reservoirs.

To further improve the fracture initiation issue, a new perforation cluster layout design is presented. It can alleviate the near wellbore fracture tortuosity issue and deliver a better oriented fracture geometry. This new perforation cluster layout can perform better if it is aligned in the optimum perforation direction. Together, this new strategy can improve the success rate of hydraulic fracture initiation or breakdown issue.

Relationship between Breakdown Pressure and Oriented Perforation for Deviated Wells

As presented in a patent by Xia and Cui (2022)[3], a framework was developed for calculating the breakdown pressure for a perforation cluster, which is applicable to deviated, cased hole, and clustered perforation hydraulic fracturing treatments. Figure 2 shows the loads that should be included to estimate the induced stresses around the wellbore perforation interface for perforation breakdown issues. First, the stresses around the perforation are induced by the far-field in situ stress tensor. Second, the borehole bottom-hole pressure, P_W, can be partially and radially transferred to the rock through casing and cement, which generates additional stresses over the wellbore perforation interface.

And third, injecting fluids into the perforation from the casing and maintaining pressure, P_{perf}, acting on the perforation wall, which generates tensile hoop stress around the perforation. It is the driving force to initiate longitudinal fracture along the perforation tunnel for a breakdown. Consequently, the fluid pressure inside the perforation tunnel can be less than the P_W inside the casing if perforation friction loss exists. The perforation friction loss can be estimated based on some empirical

Fig. 1 The orienting perforation for a horizontal well.

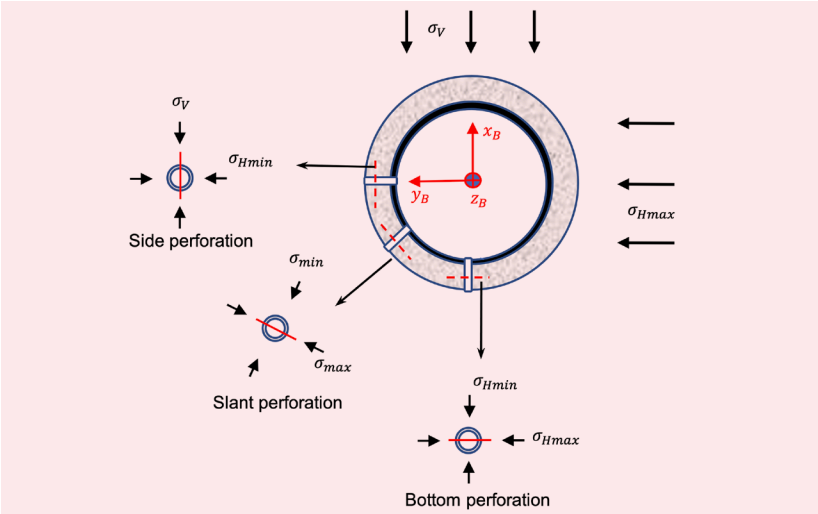

equations shown in fluid mechanics. The resulting induced stresses by these loads are denoted by superscript as σ^{I}, σ^{II}, and σ^{III}, respectively.

The breakdown pressure is estimated based on the stress state around the wellbore perforation interface. From a mechanics point of view, the breakdown pressure for a perforation cluster is a highly 3D mechanics problem and is very difficult to obtain the closed form analytical solution; however, it can be approximately obtained through iterating the phase angle from 0° to 360°. Based on the lowest breakdown pressure and its corresponding phase angle predicted by the model[3],

Fig. 2 The loads and induced stresses around the perforation tunnel wall.

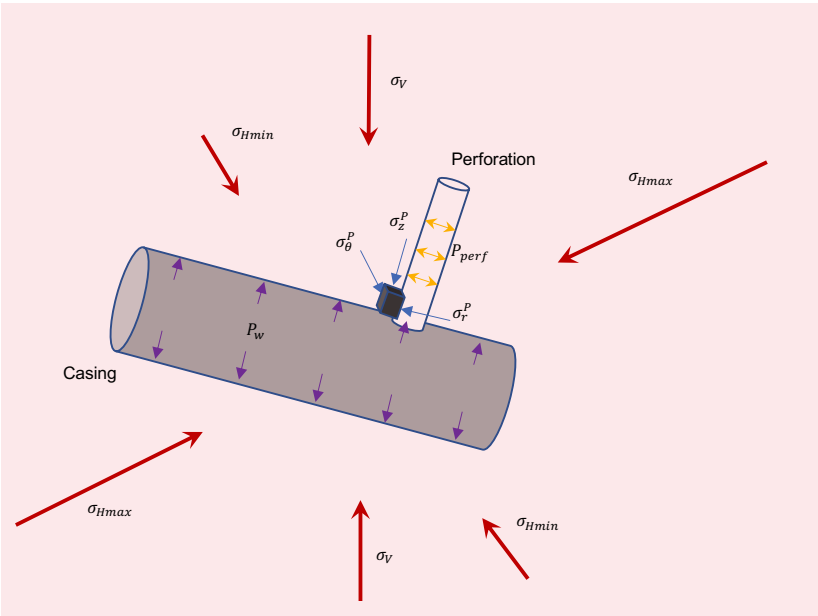

the optimum perforation azimuth and dip angle can be subsequently calculated through the coordinate system transformation. The detailed procedures to calculate the optimum perforation direction will be introduced next.

Series of Coordinate System Transformation

To predict the required breakdown pressure for hydraulic fracturing treatment, there is a need to transform the far field in situ stresses from the global coordinate system to the local coordinate system attached to each individual perforation, Fig. 3.

As shown in Fig. 3, we have the first global coordinate system, $x_G^0 y_G^0 z_G^0$, starting from the measure depth of zero. In this framework, the global coordinate system is defined as the x-axis always aligning with the north, the y-axis aligning with the east, and therefore, the z-axis is vertically downward, e.g., into the Earth. For the well survey, any point along the well trajectory can be determined by three parameters: measured depth (MD), wellbore deviation (α_D^n), and wellbore azimuth (α_A^n). At each MD along the deviated wellbore, we add a series of the global coordinate system, $x_G^n y_G^n z_G^n$, (translated from the first global coordinate system, $x_G^0 y_G^0 z_G^0$ but without any rotations), wellbore coordinate system, $x_B^n y_B^n z_B^n$, established based on the MD, α_D^n, α_A^n, and perforation coordinate system, $x_P^m y_P^m z_P^m$, considering the perforation phase angle. The wellbore coordinate system at any point along the well trajectory can be tracked and obtained by the following rotations about the global coordinate system, $x_G y_G z_G$, particularly following two steps: (1) rotation of deviation, α_D, about the y_G-axis, and (2) rotation of the azimuth, α_A, about the z_G-axis. Then the transformation matrix is given by:

$$\boldsymbol{R}_{\boldsymbol{G}\to\boldsymbol{B}}^{\boldsymbol{n}}(\alpha_A^n, \alpha_D^n) = \boldsymbol{R}_{\boldsymbol{y}}(\alpha_D^n)\boldsymbol{R}_{\boldsymbol{z}}(\alpha_A^n) =$$

$$\begin{bmatrix} \cos\alpha_D^n & 0 & -\sin\alpha_D^n \\ 0 & 1 & 0 \\ \sin\alpha_D^n & 0 & \cos\alpha_D^n \end{bmatrix} \begin{bmatrix} \cos\alpha_A^n & \sin\alpha_A^n & 0 \\ -\sin\alpha_A^n & \cos\alpha_A^n & 0 \\ 0 & 0 & 1 \end{bmatrix} \quad (1)$$

and leads to the following:

$$\boldsymbol{R}_{\boldsymbol{G}\to\boldsymbol{B}}^{\boldsymbol{n}}(\alpha_A^n, \alpha_D^n) =$$

$$\begin{bmatrix} \cos\alpha_D^n\cos\alpha_A^n & \cos\alpha_D\sin\alpha_A^n & -\sin\alpha_D^n \\ -\sin\alpha_A^n & \cos\alpha_A^n & 0 \\ \sin\alpha_D^n\cos\alpha_A^n & \sin\alpha_D^n\sin\alpha_A^n & \cos\alpha_D^n \end{bmatrix} \quad (2)$$

Also, note that the point of P_1 is always at the highest point of the wellbore cross section and will not change even following rotations of the α_D^n about the y_G^n-axis; and rotation of the α_A^n about the z_G^n-axis. Generally, the perforation direction is perpendicular to the wellbore axis and perforated at the radial direction of the wellbore. Therefore, the rotation matrix from the wellbore coordinate system to the first perforation coordinate system can be obtained by a rotation of $\alpha_{y_B}^n$ about the y_B^n-axis of the wellbore coordinate system, as follows:

$$\boldsymbol{R}(\alpha_{y_B}^m) = \begin{bmatrix} \cos\alpha_{y_B}^m & 0 & -\sin\alpha_{y_B}^m \\ 0 & 1 & 0 \\ \sin\alpha_{y_B}^m & 0 & \cos\alpha_{y_B}^m \end{bmatrix} \quad (3)$$

Rotating the y-axis of the wellbore coordinate system at any point by $\alpha_{y_B}^1 = \pi/2$, we have the first perforation coordinate system and the corresponding rotation

Fig. 3 *The coordinate systems used for transforming in situ stresses from the global coordinate system to the perforation coordinate system.*

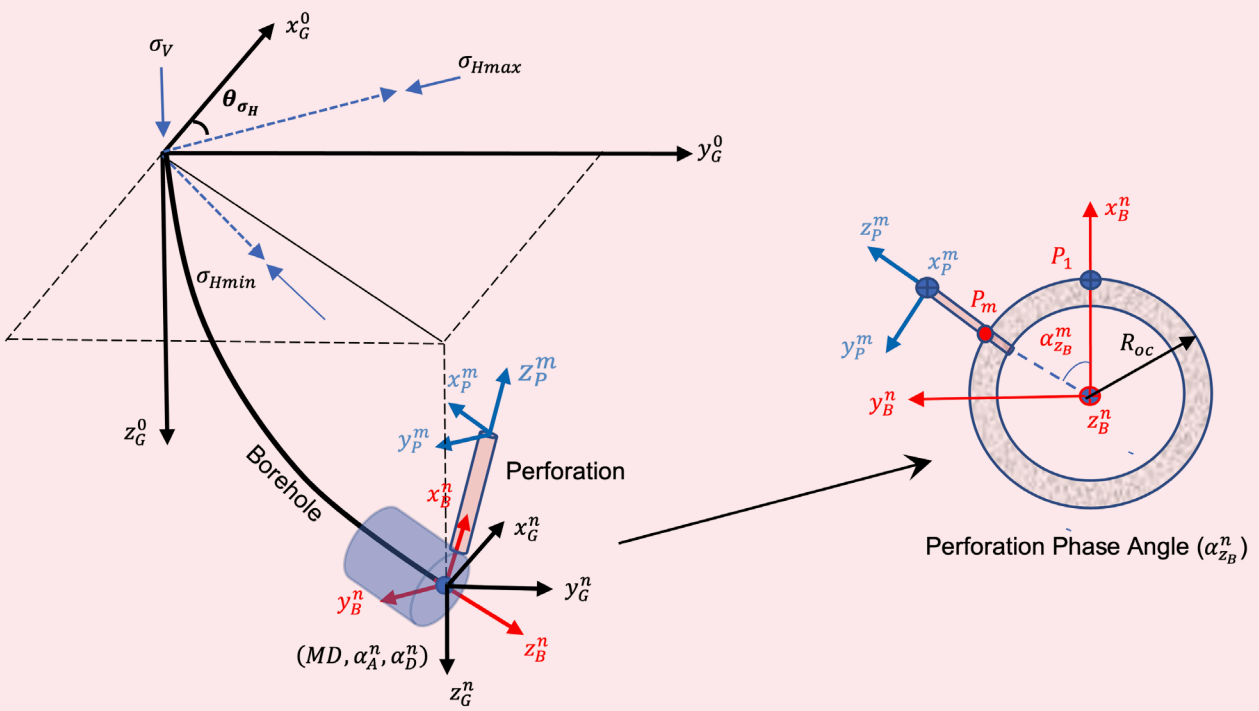

matrix as:

$$\boldsymbol{R}^{\mathbf{1}}_{\boldsymbol{B\to P}}\left(\alpha^{1}_{y_B}=\frac{\pi}{2}\right)=\begin{bmatrix}0 & 0 & -1\\ 0 & 1 & 0\\ 1 & 0 & 0\end{bmatrix} \quad 4$$

The coordinate system for different phase angle perforation can be rotated by two steps: (1) rotating $\alpha^{1}_{y_B}=\pi/2$, about the y^{n}_{B}-axis of the wellbore coordinate system; and (2) rotation of the phase angle, $\alpha^{n}_{z_B}$, about the z^{n}_{B}-axis of the wellbore coordinate system. For clustered perforations with a known perforation phase angle, the rotation matrix from $x^{n}_{B}y^{n}_{B}z^{n}_{B}$, to $x^{m}_{P}y^{m}_{P}z^{m}_{P}$, can be sequentially obtained by:

$$\boldsymbol{R}^{\boldsymbol{m}}_{\boldsymbol{B\to P}}\left(\alpha^{m}_{z_B},\alpha^{m}_{y_B}\right)=\boldsymbol{R}^{\mathbf{1}}_{\boldsymbol{B\to P}}\boldsymbol{R}_{\boldsymbol{z,B}}\left(\alpha^{m}_{z_B}\right)=$$

$$\begin{bmatrix}0 & 0 & -1\\ \sin\alpha^{m}_{z_B} & \cos\alpha^{m}_{z_B} & 0\\ \cos\alpha^{m}_{z_B} & \sin\alpha^{m}_{z_B} & 0\end{bmatrix} \quad 5$$

Therefore, the final rotation matrix from the global coordinate system to the individual perforation coordinate system can be given by:

$$\boldsymbol{R}_{\boldsymbol{G\to P}}=\boldsymbol{R}^{\boldsymbol{n}}_{\boldsymbol{G\to B}}(\alpha^{n}_{A},\alpha^{n}_{D})\boldsymbol{R}^{\boldsymbol{m}}_{\boldsymbol{B\to P}}\left(\alpha^{m}_{z_B},\alpha^{m}_{y_B}\right)=$$

$$\begin{bmatrix}R^{11}_{GP} & R^{12}_{GP} & R^{13}_{GP}\\ R^{21}_{GP} & R^{22}_{GP} & R^{23}_{GP}\\ R^{31}_{GP} & R^{32}_{GP} & R^{33}_{GP}\end{bmatrix} \quad 6$$

where $\alpha^{m}_{z_B}$ is the perforation phase angle rotating about the wellbore's z-axis starting from the highest point, Fig. 4, which ranges from 0° to 360°. By far, we introduce all the coordinate systems, which are used to project stress tensor transformation, calculating breakdown pressure. Also, it is required for calculating the optimum perforation direction. Once the lowest breakdown pressure from a perforation cluster is identified, the corresponding $\alpha^{m}_{z,B}$ will be the optimum perforation phase angle with respect to the wellbore coordinate system. For an arbitrarily deviated well, this angle might be difficult to be used for oriented perforation purposes. The perforation azimuth or perforation dip angle might be required for targeting a shaped charge gun fired in the optimum perforation direction in the subsurface.

Calculation of Perforation Azimuth

Based on the developed formulation of the breakdown pressure, we can quickly obtain the minimum breakdown pressure and its corresponding phase angle, $\alpha^{m}_{z_B}$, Fig. 4. Also note that the perforation at the angles of $\alpha^{m}_{z_B}$ and $\alpha^{m}_{z_B}+180°$ require the same amount of breakdown pressure. Therefore, the angle $\alpha^{m}_{z_B}$ can be obtained by calculating the breakdown pressure ranging from 0° to 360°. Once we find the lowest breakdown pressure for each perforation cluster, the corresponding angle $\alpha^{m}_{z_B}$ can be obtained. The perforation phase angles can be directly used to calculate the perforation azimuth and perforation dip in the translated global coordinate.

For this purpose, we calculate the azimuth and dip angle of the perforation tunnels with minimum breakdown pressure for each perforation cluster. It can be used for executing oriented perforations in a downhole operation. As indicated in Fig. 4, P_m is used to denote the intersection point of the perforation and the wellbore. The coordinates of point P_m in the wellbore coordinate system can be calculated as follows:

$$\begin{cases}x^{P_m}_{B}=R_{oc}\cos\alpha^{m}_{z_B}\\ y^{P_m}_{B}=R_{oc}\sin\alpha^{m}_{z_B}\\ z^{P_m}_{B}=0\end{cases} \quad 7$$

where R_{oc} is the radius of the cement. The coordinates of the point P_m in the wellbore coordinate system and the

Fig. 4 The projection of the wellbore's perforation intersection point on the translated global coordinate system.

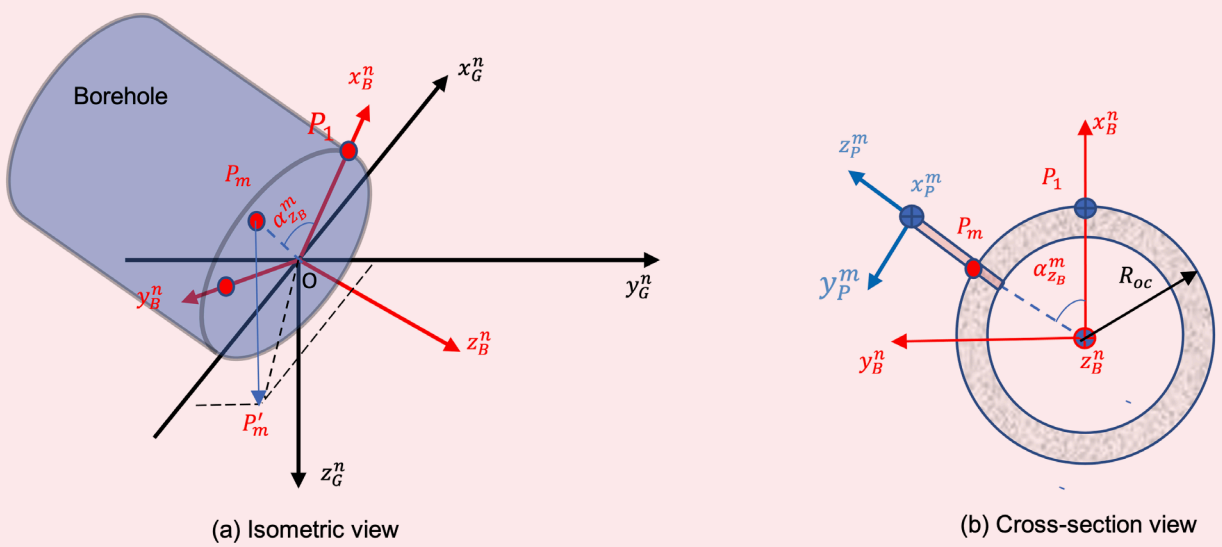

global coordinate system are transformed by:

$$\begin{Bmatrix} x_B^{P_m} \\ y_B^{P_m} \\ z_B^{P_m} \end{Bmatrix} = \begin{bmatrix} \cos\alpha_D^n \cos\alpha_A^n & \cos\alpha_D \sin\alpha_A^n & -\sin\alpha_D^n \\ -\sin\alpha_D^n & \cos\alpha_A^n & 0 \\ \sin\alpha_D^n \cos\alpha_A^n & \sin\alpha_D^n \sin\alpha_A^n & \cos\alpha_D^n \end{bmatrix} \begin{Bmatrix} x_G^{P_m} \\ y_G^{P_m} \\ z_G^{P_m} \end{Bmatrix} \quad (8)$$

Therefore, the coordinates of point P_m in the translated global coordinate system can be obtained by:

$$\begin{Bmatrix} x_G^{P_m} \\ y_G^{P_m} \\ z_G^{P_m} \end{Bmatrix} = \begin{bmatrix} \cos\alpha_D^n \cos\alpha_A^n & \cos\alpha_D \sin\alpha_A^n & -\sin\alpha_D^n \\ -\sin\alpha_D^n & \cos\alpha_A^n & 0 \\ \sin\alpha_D^n \cos\alpha_A^n & \sin\alpha_D^n \sin\alpha_A^n & \cos\alpha_D^n \end{bmatrix}^{-1} \begin{Bmatrix} x_B^{P_m} \\ y_B^{P_m} \\ z_B^{P_m} \end{Bmatrix} \quad (9)$$

The inverse of the rotation matrix can be obtained analytically or by numerical method. Once the coordinates of point P_m in the translated global coordinate system is obtained, the vectors of $\overrightarrow{OP_m}$ and $\overrightarrow{OP'_m}$ can be expressed by:

$$\overrightarrow{OP_m} = x_G^{P_m} i + y_G^{P_m} j + z_G^{P_m} k \quad (10)$$

$$\overrightarrow{OP'_m} = x_G^{P_m} i + y_G^{P_m} j \quad (11)$$

The azimuth of the perforation, which requires the least breakdown pressure, is the angle rotating clockwise from the x_G^n-axis to the vector $\overrightarrow{OP'_m}$, which is equivalent to the angle between unit vector i and vector $\overrightarrow{OP'_m}$ in the coordinate system $x_G^n y_G^n z_G^n$. Therefore, the perforation azimuth and dip can be calculated by:

$$\cos(\text{Perf\_AZI}) = \frac{i \cdot \overrightarrow{OP'_m}}{\|\overrightarrow{OP_m}\| \|\overrightarrow{OP'_m}\|} \quad (12)$$

$$\cos(\text{Perf\_Dip}) = \frac{\overrightarrow{OP_m} \cdot \overrightarrow{OP'_m}}{\|\overrightarrow{OP_m}\| \|\overrightarrow{OP'_m}\|} \quad (13)$$

Figure 5 shows the workflow for calculating the breakdown pressure and the corresponding optimum perforation direction, which is applicable to deviated wells with clustered perforation hydraulic fracturing treatment. The whole workflow can be integrated with any geoscience software, such as Tech-Log. The required parameters related to formation mechanical properties can be conveniently calculated and prepared before calculating the breakdown pressure and optimum perforation direction.

Example Study

We designed two case studies to demonstrate the analytical model performance. Table 1 shows the well trajectory, inside diameter (ID), and outside diameter (OD) of the casing, cement, and the mechanical properties for case 1. In the two case studies, we assume the maximum horizontal stress angle (azimuth) is 0°. But for each case, the well trajectory has a different well azimuth and deviation along the wellbore's trajectory. All the rest of the parameters related to casing, cement, and formation are the same for both cases.

Table 2 provides the predicted minimum breakdown pressure and the corresponding perforation phase angle and perforation azimuth along the deviated wellbore for case 1, which has a varying azimuth and deviation. Note, P_{w_min} is the minimum breakdown pressure. Phase_angle_1 and Perf_Azi_1 are the corresponding first perforation phase angle and perforation azimuth found through the model calculation. And Phase_angle_2 and Perf_Azi_2 are the corresponding second perforation phase angle and perforation azimuth through the model calculation. The two perforations have a difference of

Fig. 5 The workflow for calculating the breakdown pressure.

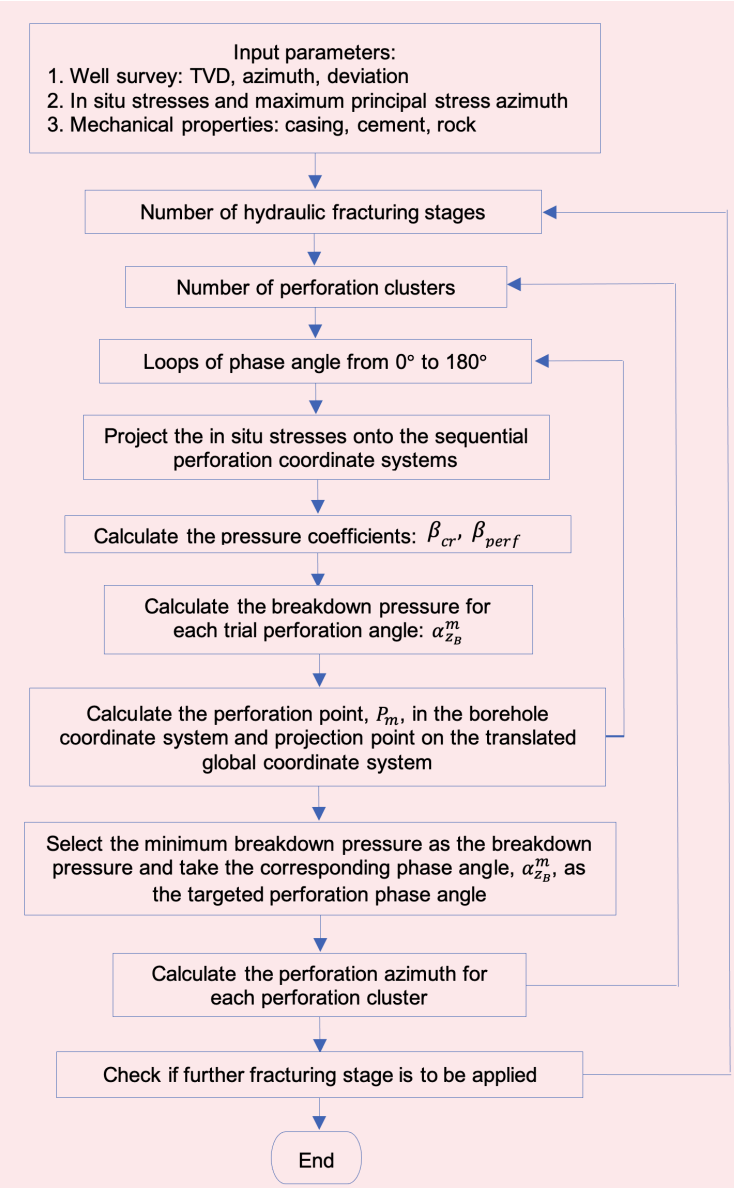

Table 1 *The well trajectory, ID, and OD of the casing, cement, and mechanical properties for case 1.*

MD (ft)	Azimuth (degree)	Deviation (degree)	Casing ID (in)	Casing OD (in)	Cement ID (in)	Cement OD (in)	Borehole ID (in)	Casing YM (psi)	Casing PR	Cement YM (psi)	Cement PR	Rock YM (psi)	Rock PR
10,000	90	10	4.09	4.5	4.5	5.875	5.875	29,000,000	0.2	250,000	0.2	3,000,000	0.22
10,500	90	20	4.09	4.5	4.5	5.875	5.875	29,000,000	0.2	250,000	0.2	3,000,000	0.22
11,000	90	30	4.09	4.5	4.5	5.875	5.875	29,000,000	0.2	250,000	0.2	3,000,000	0.22
11,500	90	40	4.09	4.5	4.5	5.875	5.875	29,000,000	0.2	250,000	0.2	3,000,000	0.22
12,000	90	50	4.09	4.5	4.5	5.875	5.875	29,000,000	0.2	250,000	0.2	3,000,000	0.22
12,500	90	60	4.09	4.5	4.5	5.875	5.875	29,000,000	0.2	250,000	0.2	3,000,000	0.22
13,000	90	70	4.09	4.5	4.5	5.875	5.875	29,000,000	0.2	250,000	0.2	3,000,000	0.22
13,500	90	80	4.09	4.5	4.5	5.875	5.875	29,000,000	0.2	250,000	0.2	3,000,000	0.22
14,000	90	85	4.09	4.5	4.5	5.875	5.875	29,000,000	0.2	250,000	0.2	3,000,000	0.22
14,500	90	90	4.09	4.5	4.5	5.875	5.875	29,000,000	0.2	250,000	0.2	3,000,000	0.22
15,000	90	95	4.09	4.5	4.5	5.875	5.875	29,000,000	0.2	250,000	0.2	3,000,000	0.22

Table 2 *The predicted phase angle and perforation azimuth for the minimum breakdown pressure for case 1.*

MD (ft)	Azimuth (degree)	Deviation (degree)	Sv (psi)	S_{hmin} (psi)	S_{hmax} (psi)	S_{hmax} Azi (degree)	PP (psi)	Pw_min (psi)	Phase Angle_1	Perf_Azi_1 (degree)	Phase_Angle_2 (degree)	Perf_Azi_2 (degree)
10,000	90	10	10,500	2,691.54	3,701.92	0	5,000	4,185.8	90	180	270	0
10,500	90	20	10,500	2,691.54	3,701.92	0	5,000	4,232.5	90	180	270	0
11,000	90	30	10,500	2,691.54	3,701.92	0	5,000	4,306.4	90	180	270	0
11,500	90	40	10,500	2,691.54	3,701.92	0	5,000	4,401.2	90	180	270	0
12,000	90	50	10,500	2,691.54	3,701.92	0	5,000	4,507.4	90	180	270	0
12,500	90	60	10,500	2,691.54	3,701.92	0	5,000	4,612.7	90	180	270	0
13,000	90	70	10,500	2,691.54	3,701.92	0	5,000	4,702.9	90	180	270	0
13,500	90	80	10,500	2,691.54	3,701.92	0	5,000	4,764	90	180	270	0
14,000	90	85	10,500	2,691.54	3,701.92	0	5,000	4,780.2	90	180	270	0
14,500	90	90	10,500	2,691.54	3,701.92	0	5,000	4,785.6	90	180	270	0
15,000	90	95	10,500	2,691.54	3,701.92	0	5,000	4,780.2	90	180	270	0

180° in their phase angle and perforation azimuth.

Table 3 shows the well trajectory, ID, and OD of the casing, cement, and the mechanical properties for case 2.

Table 4 provides the predicted minimum breakdown pressure and the corresponding perforation phase angle and perforation azimuth along the deviated wellbore for case 2.

As listed in Tables 2 and 4, perforations along the optimum direction (perforation phase angle and perforation azimuth) will require the lowest breakdown pressure for initiating transverse fractures.

New Perforation Cluster Layout Design

Once the optimum perforation direction for a perforation cluster is determined, the next task is to ensure two perforation tunnels from the same perforation cluster can be shot in the optimum perforation direction. This can be achieved through a downhole perforation control system.

Figure 6 represents the conventional perforation cluster layout design, which is widely used in today's hydraulic fracturing treatment. The perforation cluster uses the same perforation diameter for each perforation tunnel and the phase angle increases spirally at an increment of

Table 3 *The well trajectory, ID, and OD of the casing, cement, and mechanical properties for case 2.*

MD (ft)	Azimuth (degree)	Deviation (degree)	Casing ID (in)	Casing OD (in)	Cement ID (in)	Cement OD (in)	Borehole ID (in)	Casing YM (psi)	Casing PR	Cement YM (psi)	Cement PR	Rock YM (psi)	Rock PR
10,000	0	90	4.09	4.5	4.5	5.875	5.875	29,000,000	0.2	250,000	0.2	3,000,000	0.22
10,500	10	90	4.09	4.5	4.5	5.875	5.875	29,000,000	0.2	250,000	0.2	3,000,000	0.22
11,000	20	90	4.09	4.5	4.5	5.875	5.875	29,000,000	0.2	250,000	0.2	3,000,000	0.22
11,500	30	90	4.09	4.5	4.5	5.875	5.875	29,000,000	0.2	250,000	0.2	3,000,000	0.22
12,000	40	90	4.09	4.5	4.5	5.875	5.875	29,000,000	0.2	250,000	0.2	3,000,000	0.22
12,500	50	90	4.09	4.5	4.5	5.875	5.875	29,000,000	0.2	250,000	0.2	3,000,000	0.22
13,000	60	90	4.09	4.5	4.5	5.875	5.875	29,000,000	0.2	250,000	0.2	3,000,000	0.22
13,500	70	90	4.09	4.5	4.5	5.875	5.875	29,000,000	0.2	250,000	0.2	3,000,000	0.22
14,000	80	90	4.09	4.5	4.5	5.875	5.875	29,000,000	0.2	250,000	0.2	3,000,000	0.22
14,500	90	90	4.09	4.5	4.5	5.875	5.875	29,000,000	0.2	250,000	0.2	3,000,000	0.22
15,000	100	90	4.09	4.5	4.5	5.875	5.875	29,000,000	0.2	250,000	0.2	3,000,000	0.22

Table 4 *The predicted phase angle and perforation azimuth for the minimum breakdown pressure for case 2.*

MD (ft)	Azimuth (degree)	Deviation (degree)	Sv (psi)	S_{hmin} (psi)	S_{hmax} (psi)	S_{hmax} Azi (degree)	PP (psi)	Pw_min (psi)	Phase Angle_1	Perf_Azi_1 (degree)	Phase_Angle_2 (degree)	Perf_Azi_2 (degree)
10,000	0	90	10,500	2,691.54	3,701.92	0	5,000	7,210.1	90	90	270	270
10,500	10	90	10,500	2,691.54	3,701.92	0	5,000	7137	90	100	270	280
11,000	20	90	10,500	2,691.54	3,701.92	0	5,000	6,926.5	90	110	270	290
11,500	30	90	10,500	2,691.54	3,701.92	0	5,000	6,604	90	120	270	300
12,000	40	90	10,500	2,691.54	3,701.92	0	5,000	6,208.4	90	130	270	310
12,500	50	90	10,500	2,691.54	3,701.92	0	5,000	5,787.4	90	140	270	320
13,000	60	90	10,500	2,691.54	3,701.92	0	5,000	5,391.8	90	150	270	330
13,500	70	90	10,500	2,691.54	3,701.92	0	5,000	5,069.2	90	160	270	340
14,000	80	90	10,500	2,691.54	3,701.92	0	5,000	4,858.8	90	170	270	350
14,500	90	90	10,500	2,691.54	3,701.92	0	5,000	4,785.6	90	180	270	0
15,000	100	90	10,500	2,691.54	3,701.92	0	5,000	4,858.8	90	190	270	10

60°. Using this conventional perforation cluster layout design, together with the oriented perforation technique, the two perforations aligning in the optimum perforation direction are not the closest to each other. There are two additional perforation tunnels between them, which can lead to near wellbore fracture tortuosity and premature screen out. Therefore, it is not the best layout of the perforation cluster design.

To further overcome the weakness of the existing perforation cluster layout, we present a new perforation cluster layout design, Fig. 7[4]. Figure 8 shows the orientation of the new perforation cluster layout in a subsurface geologic setting. For this new perforation cluster layout design, the two perforation tunnels (#1 and #2) in the middle of the perforation clusters, have larger perforation diameters. Also, they are close to each other and have a phase angle difference of 180°. As noted in Fig. 8, they should be aligned in the optimum perforation direction based on the calculation for a well trajectory and in situ stress state. To do this, the required breakdown pressure for fracture initiation can be lowered to some extent.

The new perforation design working together with the oriented perforation calculation clearly has the following features and advantages:

Fig. 6 *The conventional perforation cluster layout design.*

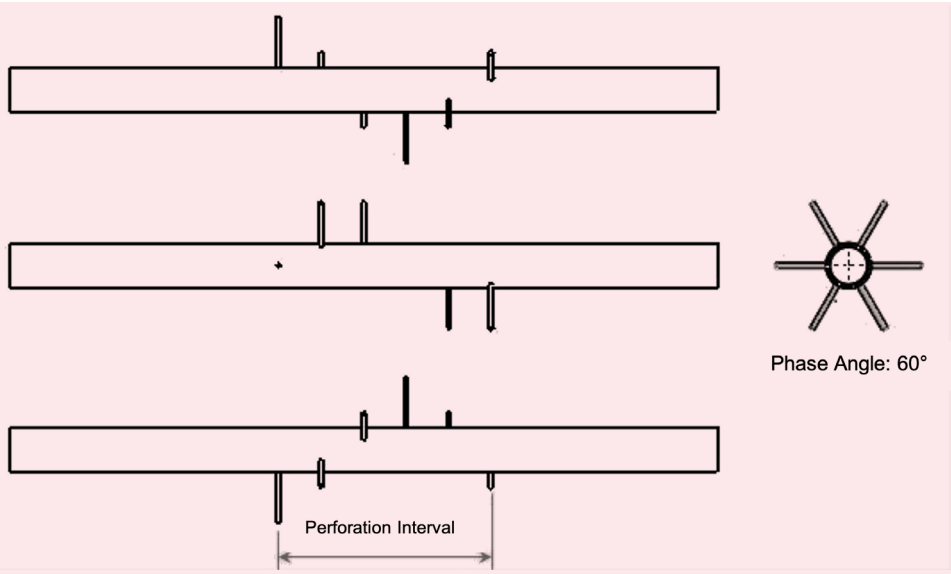

Fig. 7 *The new perforation cluster layout design with a nonuniform perforation diameter — the #1 and #2 perforation tunnels have a larger diameter.*

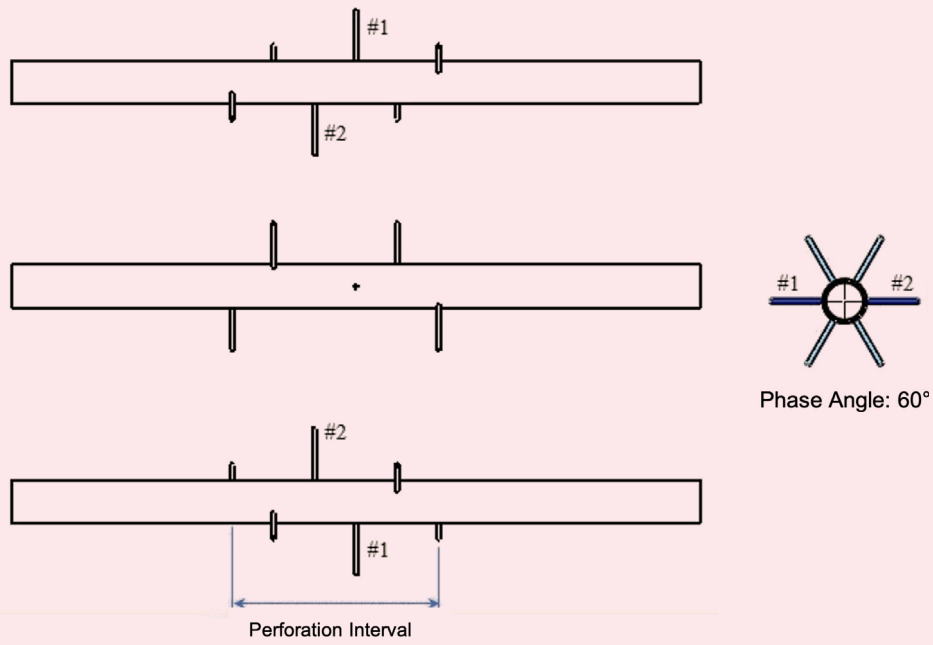

- The perforation cluster uses a nonuniform perforation diameter.
- The two perforation tunnels aligning in the optimum perforation direction have a relative larger perforation diameter; the rest of the perforation tunnels use a relative smaller diameter. The advantages of this design can ensure injection fluids flow into the perforation tunnels aligning in the optimum perforation direction as much as possible, which can boost the success rate of any breakdown issue.
- The two perforation tunnels aligning in the optimum perforation direction are next and closest to each other along the wellbore direction. Compared to the conventional design, these can alleviate the near wellbore fracture tortuosity issue, and minimize flow restriction and friction pressure loss during hydraulic

Fig. 8 *The orientation of the new perforation cluster layout design in a subsurface geologic setting.*

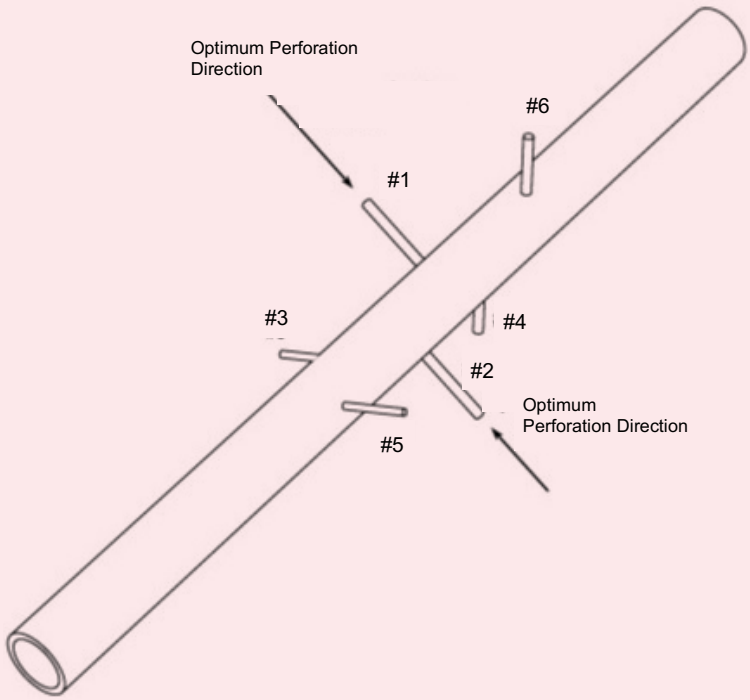

fracturing. Otherwise, multiple and reoriented nonplanar fractures originated from the wellbore perforation cluster likely lead to a premature screen out and negatively impact the fluid injection potential to achieve a desired stimulation performance.

- Combing the new perforation cluster layout design, and with the optimum perforation direction being calculated together, this can reduce the number of perforation tunnels required for each perforation cluster, unlike the currently used cluster in a hydraulic fracturing treatment. To generate the desired perforation cluster layout design, we have to adjust the shaped charge layout in the perforating gun.

The two central charges in the more explosive region are larger than the remaining charges on either side of the central charges. This is to create a perforation pattern in the wellbore whose central perforations have a larger diameter than the remaining perforations on either side of the central perforations.

Conclusions

Hydraulic fracture initiation can be a challenging issue for fracturing deep and tight gas reservoirs, which generally requires a high breakdown pressure for fracture initiation. Oriented perforation represents another approach to improve the breakdown issue, which cannot only lower the breakdown pressure to some extent, but also deliver a better oriented fracture geometry.

In this article, we first present an approach to calculate the optimum perforation direction. The method introduces a series of coordinate systems to transform the stresses for calculating breakdown pressure as well as for oriented perforation. Once the minimum breakdown pressure is determined, the corresponding perforation phase angle can be identified. Then, the perforation points in the wellbore coordinate system can be identified. Following that, the corresponding perforation azimuth and perforation dip angle with respect to the translated global coordinate system can be calculated, which represents the optimum perforation direction. Once the optimum perforation direction for a perforation cluster is determined, the next task is to ensure two perforation tunnels from a perforation cluster are aligning in the optimum perforation direction in the subsurface.

To further improve the breakdown issue, we also present a new perforation cluster layout design in this article. For this layout design, the two perforation tunnels in the middle of the perforation clusters have a larger perforation diameter. The two perforation tunnels are close to each other and have a phase angle difference of 180°. In a subsurface setting, they will be aligned in the optimum perforation direction based on the calculation for a particular geologic setting. All these will work resonantly together and improve the breakdown issue. Consequently, it can alleviate the near wellbore fracture tortuosity issue, minimize flow restriction, and pressure friction loss for hydraulic fracturing treatment. Otherwise, multiple and reoriented nonplanar fractures originated from the wellbore perforation cluster will likely lead to a premature screen out and negatively impact the fluid injection potential to achieve a desired stimulation performance.

References

1. Abass, H.H., Brumley, J.L. and Venditto. J.J.: "Oriented Perforation — A Rock Mechanics View," SPE paper 28555, presented at the SPE Annual Technical Conference and Exhibition, News Orleans, Louisiana, September 25-28, 1994.
2. Benavides, S.P., Myers, W.D., van Sickle, E.W. and Vargervik, K.: "Advances in Horizontal Oriented Perforating," SPE paper 81051, presented at the SPE Latin American and Caribbean Petroleum Engineering Conference, Port-of-Spain, Trinidad, West Indies, April 27-30, 2003.
3. Xia, K. and Cui, Y.: "Determining a Subterranean Formation Breakdown Pressure," U.S. Patent 11,255,184, February 22, 2022.
4. Xia, K.: "Perforation Cluster Layout Design and Its Relative Orientation in Subsurface for a Hydraulic Fracturing Treatment," U.S. Patent Application 17/457,567, filed on December 4, 2021.

About the Authors

Dr. Kaiming Xia

Ph.D. in Computational Mechanics,
University of Illinois at Chicago

Dr. Kaiming Xia is a Geophysicist working in Saudi Aramco's Gas Reservoir Characterization Department. His current focus is related to geomechanics and hydraulic fracturing treatment.

Prior to joining Saudi Aramco in 2019, Kaiming had worked with Caterpillar, Colorado School of Mines, Weatherford, and Shell Oil Company in the U.S. His expertise has been on multidisciplinary areas, including finite element modeling, geomechanics, soil/machine interactions, ground vehicle dynamics, downhole tool development, drilling dynamics, borehole stability, and hydraulic fracturing treatment.

Kaiming has published over 50 journal and conference papers.

He received his Ph.D. degree in Computational Mechanics from the University of Illinois at Chicago, Chicago, IL.

Dr. Yufeng Cui

Ph.D. in Geology,
China University of Petroleum

Dr. Yufeng Cui is a Geologist working on the focus area of advanced petrophysics and integrated process-based geological modeling at the Beijing Research Center or Aramco's Far East Business Services Co. Ltd.

He has authored 20 journal and conference papers, and six patent applications (with two granted so far).

In 2017, Yufeng received his Ph.D. degree in Geology from China University of Petroleum, Beijing, China.

Dr. Tariq Mahmood

Ph.D. in Geology,
University of Adelaide

Dr. Tariq Mahmood joined Saudi Aramco in 2008 and currently works in the Gas Reservoir Characterization Department as a Geological Consultant. He began his career in 1996, working in Perth, Australia, specializing in fractures/faults characterization from borehole images. Tariq has provided consultancies to major oil companies in the Asia Pacific region and Australia, including Shell Brunei, Petronas, Chevron, Santos, Apache, Woodside, etc. Since joining Saudi Aramco, he has worked on many interesting projects addressing a variety of problems in both offshore and onshore gas fields.

Tariq is a member of the American Association of Petroleum Geologists (AAPG), the European Association of Geoscientists and Engineers (EAGE), and the Dhahran Geosciences Society (DGS). He is the coauthor of three patents.

Tariq received his Ph.D. degree in Geology from the University of Adelaide, Adelaide, South Australia, Australia, in 1996. Based on his Ph.D. research, an atlas on the "3D Analogue Modeling of Extensional Fault Systems plus Field Applications" was published by the University of Adelaide. Tariq was the recipient of the Harold Rhoda Scholarship during his studies in Australia.